Journal of Building Engineering 120 (2026) 115600

Contents lists available at ScienceDirect

Journal of Building Engineering

journal homepage: www.elsevier.com/locate/jobe

Assessment and design of RC frames incorporating effects of restraint to beam hysteresis elongation

Zi-Nan Wu [a,b], Xiao-Lei Han [b], Ahmed Y. Elghazouli [a,c,*], Cunbiao Huang [b]

[a] Department of Civil & Environmental Engineering, Hong Kong Polytechnic University, Hong Kong
[b] School of Civil Eng. & Transportation, South China University of Technology, Guangzhou, China
[c] Department of Civil & Environmental Engineering, Imperial College London, UK

ARTICLE INFO

Keywords:
Seismic design
RC frames
Cyclic loading
Hysteresis elongation
Restraint effects

ABSTRACT

In reinforced concrete (RC) frames, beam elongation under cyclic loading is typically restrained by columns, hence inducing axial compression that results in beam overstrength and elevated force demands on adjacent columns and joints. Despite the pronounced influence of these restraint effects, they are not explicitly addressed in current seismic design procedures due to the lack of reliable methods for estimating the beam axial restraint stiffness and the resulting compression. To address this, a thermal analogy approach to evaluate the restraint stiffness is proposed and validated against cyclic test results. A prediction model is also developed for determining the restraint-induced axial compression, with due account for the degradation caused by column yielding. Based on these developments, a seismic design methodology that incorporates the beam axial compression effects is established. The proposed methodology is applied to a multi-story RC frame and compared with detailed numerical results. It is shown that the proportion of restraint-induced force demands increases from the frame center toward the edges. Importantly, despite employing various capacity design amplification factors, design codes are found to grossly underestimate these effects by up to 50%, particularly for shear demands in exterior columns. Considerable beam overstrength are also shown to occur in code-designed frames, with interior beams exhibiting overstrength approaching 40%. In contrast, the methodology proposed in this study effectively mitigates the beam overstrength and captures the restraint-induced force demands on both the columns and joints. By dealing with the restraint effects through beam reinforcement optimization and column-joint strengthening, the proposed methodology enables the mobilization of the intended strong-column/weak-beam and strong-joint mechanisms, hence offering a rational and practical solution for significantly improving the seismic performance of RC frame structures.

1. Introduction

Seismic design of reinforced concrete (RC) frame structures widely follows the strong-column/weak-beam philosophy, ensuring that beam yielding precedes column yielding, and enabling plastic hinges at beam ends to effectively dissipate energy [1–3]. During cyclic loading, inelastic deformations at beam hinges result in hysteresis axial elongation [4,5]. This elongation comprises two components: a recoverable geometric component caused by curvature-induced neutral axis shifts, and an irrecoverable residual

* Corresponding author. Department of Civil & Environmental Engineering, Imperial College London, UK.
E-mail address: a.elghazouli@imperial.ac.uk (A.Y. Elghazouli).

https://doi.org/10.1016/j.jobe.2026.115600
Received 5 September 2025; Received in revised form 3 February 2026; Accepted 10 February 2026
Available online 12 February 2026
2352-7102/© 2026 The Authors. Published by Elsevier Ltd. This is an open access article under the CC BY license (http://creativecommons.org/licenses/by/4.0/).

component primarily resulting from accumulated tensile plastic strains and bond-slip of longitudinal reinforcement [6]. Both components increase with hinge rotation, leading to significant elongation, typically ranging from 2% to 4% of the beam height before concrete crushing is reached [7,8].

Within a frame system, this beam elongation is restrained by adjacent columns, generating axial compression [9–15]. Cyclic tests by Kokusho et al. [9], Yang et al. [10], and Wang et al. [11] demonstrated that such restraint to elongation leads to notable axial compression, resulting in ductility reduction and substantial beam flexural overstrength typically ranging from 74% to 155%. Beyond these localized effects, restraint-induced axial compression and the associated overstrength significantly amplify the force demands on adjacent columns and joints [6,11,16–20]. Tests by Wang et al. [11] and Luo et al. [16] on RC beam-column subassemblies showed increases in joint shear demands by 61%–120%, resulting in severe joint damage. Kim et al. [20] reported shear demand increases of 80.2% and 39.1% in exterior and interior joints, respectively, and found that a beam-to-column strength ratio of 5.86 was required to prevent premature yielding of exterior columns. Numerical analyses by Wu et al. [6] further revealed that moment demands on exterior columns increased by 241%–302%, with the axial compression contributing more significantly than beam overstrength. These findings consistently point to restraint-induced axial compression as being the primary mechanism underlying elongation restraint effects, including beam overstrength, elevated joint shear demands, and increased column force demands.

To mitigate these adverse consequences, reliable estimation of the beam axial restraint stiffness is essential. Existing approaches primarily include nonlinear pushover analysis [19] and unit force-based elastic analysis [16]. In pushover analysis (Fig. 1a), restraint stiffness is derived from the beam axial force-elongation response, typically providing reasonable accuracy. However, the need for demanding nonlinear inelastic analysis limits its practicality for practical design application. Alternatively, the unit-force method (Fig. 1b) evaluates the restraint stiffness through elastic analysis by applying equal and opposite horizontal forces at the beam ends, using the assumption of uniform axial compression. Despite being relatively simple and efficient, this approach fails to capture the realistic deformation patterns, such as the development of axial tension in upper-story beams observed in pushover results, and introduces errors by requiring beam removal, which alters the overall structural stiffness. Therefore, an efficient and reliable method for estimating axial restraint stiffness is lacking.

The estimation of restraint-induced beam axial compression, the primary mechanism underlying elongation restraint effects, is also equally critical. Nonetheless, despite its importance, prediction models are also lacking. Experimental studies [9–11,16] have only investigated a limited range of restraint stiffness, and hence provide only limited insight into its relationship with the axial compression. Parametric assessments using validated models are therefore essential to quantify and establish this relationship. Moreover, both experimental and numerical studies typically assume a constant restraint stiffness throughout loading. Under such assumptions, the maximum axial compression is typically adopted to assess the beam overstrength and increased force demands on adjacent components. However, experiments have shown that full development of axial compression requires substantial plastic hinge rotations, corresponding to story drift ratios of up to 4.0% [11,16], which far exceed the column yield limits [21–23]. Once columns yield, the associated degradation in lateral stiffness reduces the restraint stiffness, thereby limiting further development of axial compression. Therefore, using the maximum axial compression in design leads to significant overestimation. Prediction models should therefore account for restraint degradation effects caused by column yielding.

Due to the absence of reliable methods for estimating the beam axial restraint stiffness and the resulting axial compression, current seismic design provisions fail to mitigate the beam elongation restraint effects. To address these gaps, this study proposes a thermal analogy approach (Fig. 1c) for estimating the axial restraint stiffness. The procedure is validated against the results of a cyclic test on an RC frame, as described in Section 2 of this paper. A model for determining the restraint-induced axial compression, with due account for restraint degradation effects due to column yielding, is subsequently proposed in Section 3. Based on these developments, Section 4 describes a suggested seismic design methodology incorporating beam reinforcement optimization and column–joint strengthening procedures that explicitly account for beam axial compression effects. The proposed methodology is applied to a prototype multi-story RC frame in Section 5. Cyclic analysis results confirm its effectiveness in mitigating beam overstrength and capturing the restraint-induced force demands on columns and joints, thereby enabling the mobilization of the intended strong-column/weak-beam and strong-joint mechanisms and ultimately enhancing the seismic performance of RC frame structures.

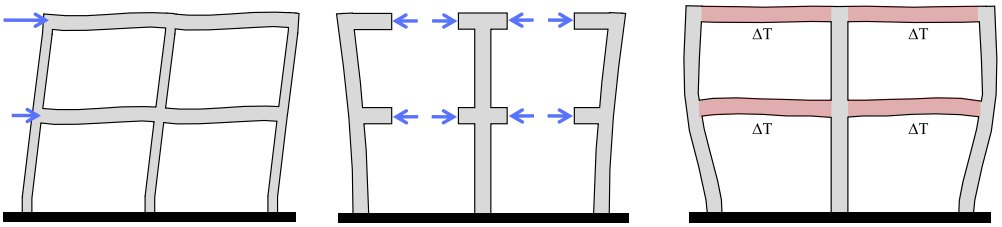


Fig. 1. Methods for estimating beam axial restraint stiffness.

2. Determination of beam axial restraint stiffness

2.1. Thermal analogy approach

To enable efficient estimation of beam axial restraint stiffness, a thermal analogy approach (Fig. 1c) is proposed herein. In this approach, beam elongation behavior is simulated by applying a uniform temperature increment ΔT to induce thermal expansion. The resulting elongation is expressed as:

$$\delta_E = \alpha \cdot \Delta T \cdot L \tag{1}$$

Where α denotes the thermal expansion coefficient, taken as 10 $\mu\varepsilon/^{\circ}$C for RC components according to standards [24], and L represents the beam span.

Fig. 2 depicts the development of elongation δ_E relative to plastic hinge rotation θ_r derived from a previous experimental investigation by the authors [6], involving beams with varying section heights h, spans L, and longitudinal reinforcement ratios ρ_l. As shown in Fig. 2a, for beams with the same h, the δ_E-θ_r curves corresponding to different L and ρ_l converge into a narrow band, indicating that these parameters influence elongation primarily through their effects on hinge rotation capacity. Fig. 2b further shows that normalizing δ_E by h leads to a closer convergence of the curves across different h values, indicating that the normalized elongation δ_E/h exhibits limited variation for a given plastic hinge rotation θ_r. These observations support the simplification of the unrestrained beam elongation as primarily a function of plastic hinge rotation and section height. This finding is consistent with formulations adopted in the literature [25] and in the New Zealand design provisions [26]. Accordingly, the elongation associated with a given plastic hinge rotation is expressed as:

$$\delta_E(\theta_r, h) = f(\theta_r)\, h \tag{2}$$

Where $f(\theta_r)$ is a normalized elongation function. By equating Eqs. (1) and (2), the required temperature increment to reproduce the elongation is derived as:

$$\Delta T(\theta_r, h, L) = \frac{f(\theta_r)}{\alpha}\frac{h}{L} \tag{3}$$

Following the application of the temperature field, linear elastic thermal analysis is employed to evaluate the restraint-induced axial forces and deformations for each beam, from which the axial restraint stiffness is estimated. Under elastic conditions, both the axial forces and deformations scale linearly with the magnitude of the applied temperature field. As a result, the computed restraint stiffness remains unchanged with respect to uniform scaling of the entire temperature field, enabling the use of a normalized temperature field in the analysis. By assuming uniform hinge rotation among all beams within the frame, the ΔT values are defined as inversely proportional to the span-to-depth ratio L/h. A reference ΔT of 1 °C is assigned to a benchmark beam with L/h of 1.0, and the ΔT values for beams are obtained by proportional scaling according to their individual L/h values. Furthermore, to account for stiffness degradation caused by tensile cracking during hinge rotation, the concrete elastic modulus of the beams is reduced by a factor of 0.4, as typically recommended by standards [24].

Compared to pushover analysis, the proposed thermal analogy approach significantly reduces computational demands by avoiding nonlinear simulations. Furthermore, unlike the unit-force method, it does not require the removal of beam elements, thereby simplifying implementation and preserving the structural stiffness integrity, which enhances its reliability.

The proposed thermal analogy approach is validated below through comparison with results obtained from detailed numerical simulations as well as cyclic loading tests.

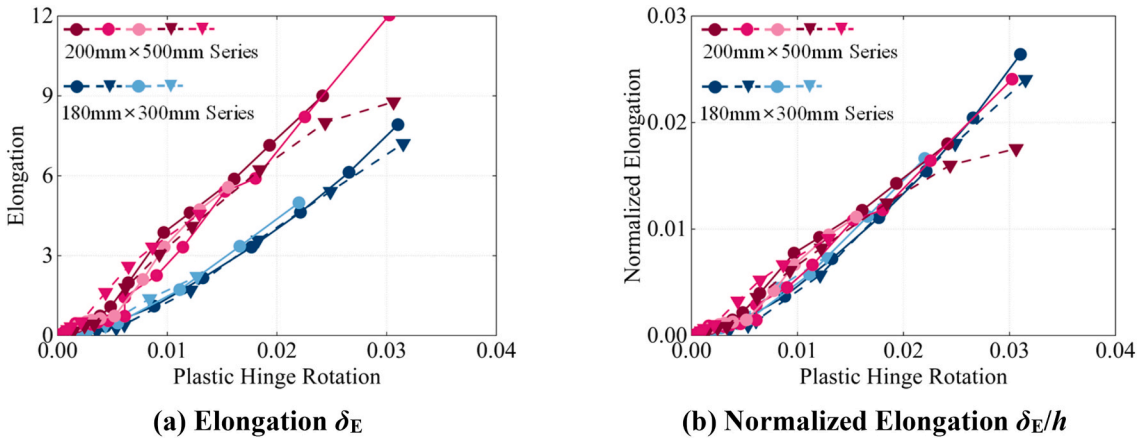


Fig. 2. Development of elongation relative to plastic hinge rotation.

2.2. Numerical modeling

Among existing nonlinear analysis methods, fiber-based distributed plasticity models [27–29] are widely used due to their computational efficiency. However, these models are based on the plane-section assumption, which limits their ability to capture truss action, a critical mechanism contributing to hysteresis elongation. Strut-and-tie models [30–32] address this limitation by explicitly modeling force transfer paths, yet their accuracy depends on user-defined parameters including crack angles and strut widths. Smeared crack models [33–35] offer a more objective alternative by incorporating concrete panels with either fixed or rotating crack angle assumptions. However, no prior studies have employed smeared crack models to simulate beam elongation and associated restraint effects until the development of the fixed-strut-angle smeared crack model with bond-slip (FSAM-BS) [6] in OpenSees [36]. This model, recently enhanced by the authors, integrates bond-slip effects into the original FSAM framework [37], thereby enabling accurate simulation of hysteretic response in terms of lateral resistance, axial elongation, and restraint-induced compression.

In this study, the FSAM-BS in OpenSees is employed, and its effectiveness is further verified against the results of a cyclic loading test on a RC frame. The restraint-induced axial compression predicted by the FSAM-BS numerical simulations is used to estimate the beam axial restraint stiffness. This is then compared with the corresponding values derived using the proposed thermal analogy method to evaluate its accuracy and applicability.

2.3. Experimental validation

The validation was carried out against the results of a two-story, two-bay RC frame test undertaken by Ning et al. [38], as illustrated in Fig. 3. The specimen had a story height of 1.44 m, resulting in a total height of 2.88 m. The columns had a cross section of 160 mm × 160 mm, and the beams of 100 mm × 200 mm. The net spans of the left and right beams were 2240 mm and 1440 mm, corresponding to span-to-depth ratios of 11.2 and 7.2, respectively. The concrete compressive strengths f_c were 28.4 MPa and 25.1 MPa for the first and second stories, with corresponding elastic moduli E_c of 28.5 GPa and 26.4 GPa. The yield strengths of the longitudinal reinforcement f_y in beams and columns were 304 MPa and 384 MPa, respectively, while that of stirrups f_{yv} was 294 MPa. Lateral loading through displacement control was applied at the top of the frame.

The finite element model was developed in OpenSees and is illustrated in Fig. 4. Membrane fiber elements developed by López et al. [39] were utilized, in which the FSAM-BS was employed for beams, while the original FSAM formulation was used for columns. To ensure deformation compatibility at beam–column interfaces, the column elements were discretized with mesh widths of 0.5 times the section height (80 mm), while the beam elements used a finer mesh with widths of 0.25 times the section height (50 mm). Two RC panels were assigned across the width of each element. As shown in Fig. 4b, both FSAM and FSAM-BS follow the same underlying principles [40], consisting of three stages: uncracked, post-initial cracking, and post-secondary cracking. In the uncracked stage, a rotating-angle approach is applied. Once the first crack forms, the model transitions to a fixed-angle mechanism to represent crack development and force transfer.

Concrete behavior in both beams and columns was described using the constitutive model proposed by Chang and Mander [41], as shown in Fig. 4c. This model is defined by the elastic modulus (E_c), the compressive and tensile peak coordinates (ε_c, f_c and ε_t, f_t), and corresponding shape coefficients (r_c, r_t). The parameters E_c, ε_c, and ε_t were determined according to standards [24] based on the measured f_c and f_t. The coefficient r_c was obtained from empirical expressions [41], while r_t was taken as 1.2 following the recommendations of Orakcal and Wallace [42].

The hysteretic behavior of reinforcement was modeled using the Menegotto-Pinto relationship [43], as illustrated in Fig. 4d. This model is characterized by the elastic modulus (E_s), yield strength (f_y), strain hardening ratio (α_s), and curvature parameters (R_0, a_1, a_2). The parameters E_s and α_s were determined according to standards [24] based on the measured f_y, while the curvature parameters were adopted as $R_0 = 20$, $a_1 = 18.5$, $a_2 = 0.15$, consistent with commonly used recommendations [43].

The FSAM-BS model further incorporates a bond-slip mechanism [6], as shown in Fig. 4e. This mechanism is governed by recoverable and irrecoverable bond-slip coefficients (ζ_e, ζ_p), which were determined using previously proposed relationships [6].

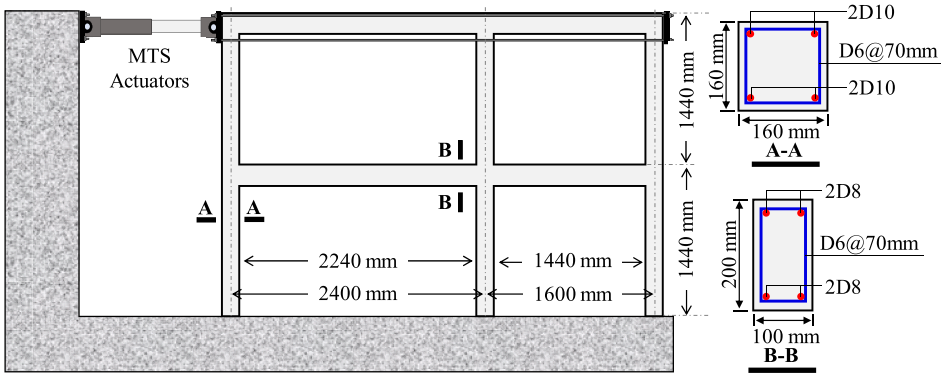


Fig. 3. Geometry and details of the RC frame specimen tested under cyclic loading [38].

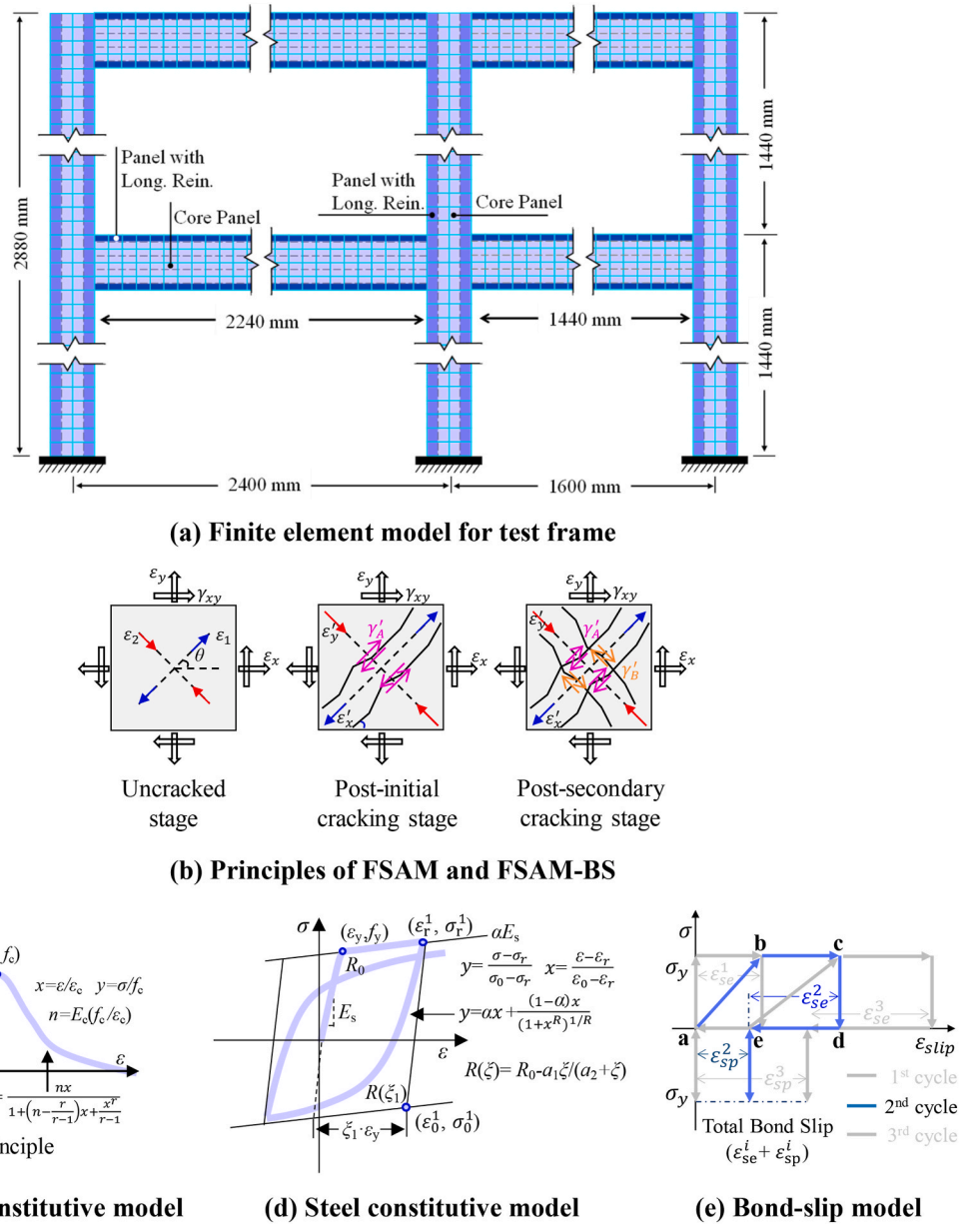


Fig. 4. Finite element model incorporating FSAM and FSAM-BS for RC frame.

2.4. *Validation of numerical modeling*

Fig. 5 compares the experimental and predicted cyclic response as well as energy dissipation and secant stiffness for the hysteretic cycles. The results demonstrate that the numerical model accurately captures the lateral load resistance, energy dissipation, and stiffness degradation of the RC frame. Fig. 6 further compares the experimental [38,44] and predicted crack patterns of the RC frame at the end of the loading protocol. Extensive flexural cracking was observed in both beams and columns. At the first story, fully developed flexural cracks appeared at the beam ends and column bases. At the second story, fully developed flexural cracks were observed at the top of the interior columns, indicating yielding of the longitudinal reinforcement. This column yielding restricted the plasticity development of the adjacent beam ends, resulting in the absence of significant flexural cracks in those regions. The numerical model effectively captured these features and observed crack patterns.

The crack patterns also revealed distinct differences between interior and exterior columns at the first story. Bi-directional flexural cracks developed at the ends of interior columns connected to first-story beams, whereas only one-directional flexural cracks were observed at the corresponding ends of exterior columns. Similar observations have been reported in previous experimental and numerical studies on beam–column subassemblies [6,20] and are primarily attributed to the effects of restraint-induced beam axial

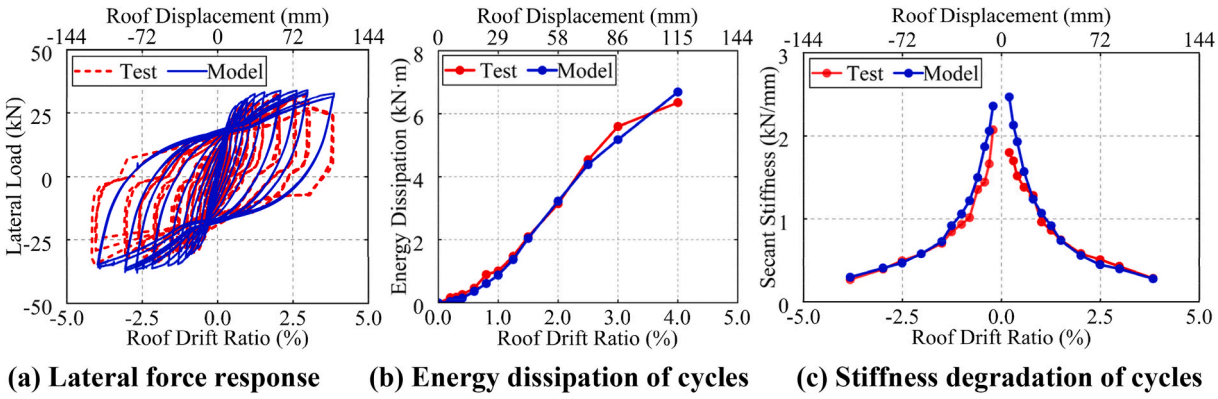


Fig. 5. Comparison of experimental and predicted hysteretic responses of the RC fame.

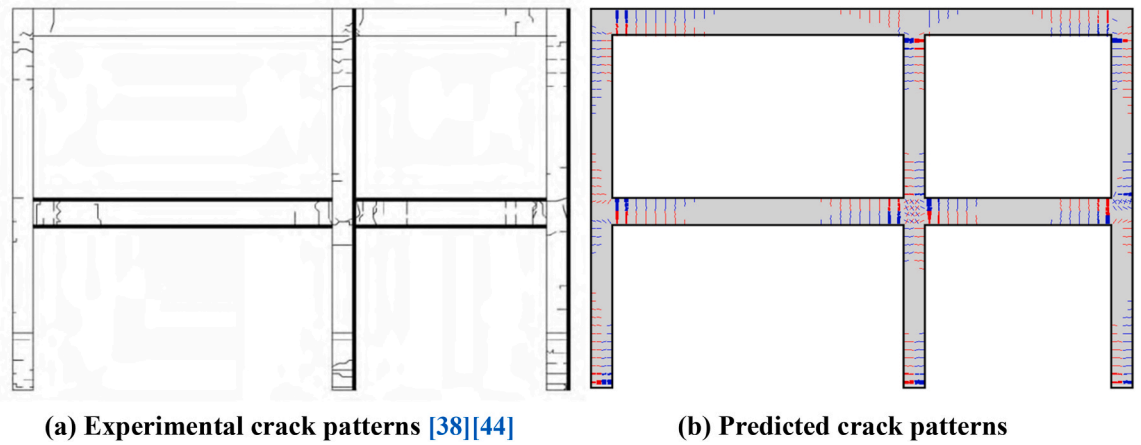


Fig. 6. Comparison of experimental and predicted crack patterns in the RC frame.

compression. To elucidate this mechanism, Fig. 7 compares the moment diagrams of the left exterior column at the onset of column yielding, with and without restraint-induced beam axial compression. Because beam elongation accumulates progressively under cyclic loading, the associated restraint-induced shear and moment demands imposed on the columns do not reverse with the loading direction, unlike the lateral load–induced forces. When the restraint-induced shear accounts for a substantial portion of the total column shear, it markedly modifies the moment distribution, causing the column-end moments connected to first-story beams to remain unidirectional and resulting in one-directional flexural cracking. In contrast, for interior columns, restraint-induced axial compression from beams on both sides are partially counteracted, reducing its influence on the moment distribution. Consequently, column moments continue to reverse with the loading direction, leading to bi-directional flexural cracking.

2.5. *Assessment of restraint stiffness*

Fig. 8 presents the hysteretic relationships between restraint-induced axial force and beam elongation. For clarity, the first-story

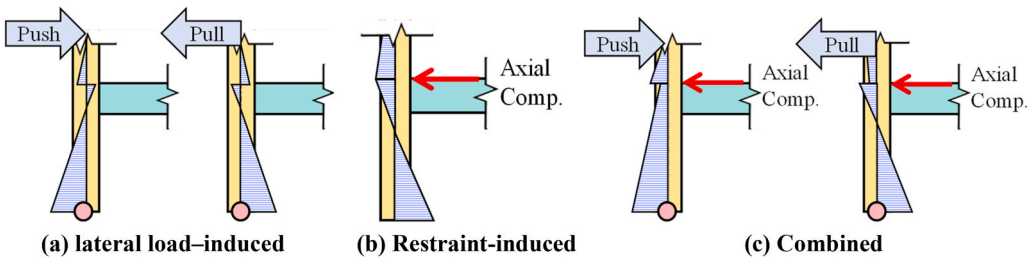


Fig. 7. Moment diagrams of the exterior column at column yielding.

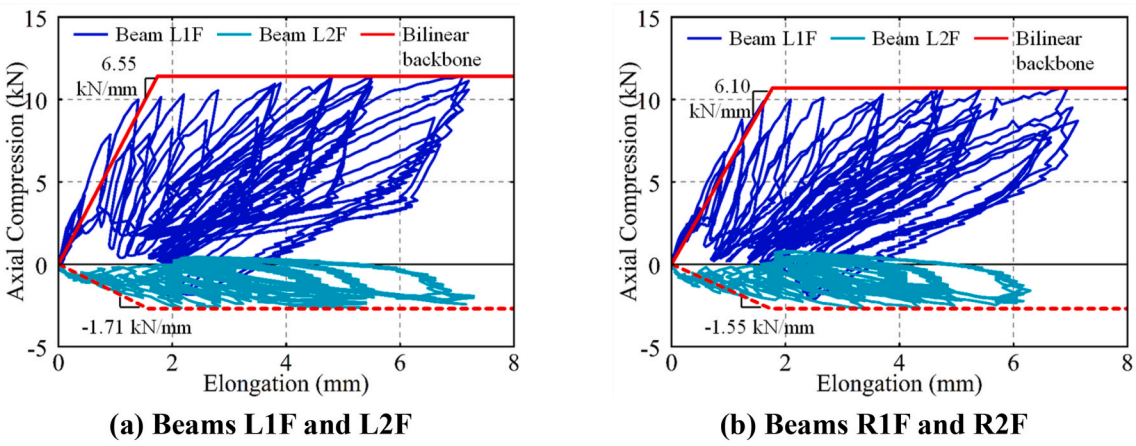


Fig. 8. Hysteretic relationships between restraint-induced axial force and beam elongation.

left and right beams are denoted as Beams L1F and R1F, while the second-story left and right beams are denoted as Beams L2F and R2F. The results indicate that the first-story beams experienced axial compression due to the restraint from surrounding components. In contrast, although the second-story beams also experienced elongation, they provided additional restraint to the elongation of the first-story beams, thereby developing axial tension. The magnitude of this tension was approximately 25% of the axial compression observed in the first-story beams.

To quantify the axial restraint stiffness K_r, an elasto-plastic bilinear backbone curve was fitted to the hysteretic responses based on energy equivalence. A positive K_r value is associated with axial compression developed during beam elongation, whereas negative value corresponds to axial tension. The analysis resulted in K_r values of 6.55 kN/mm for Beam L1F and 6.05 kN/mm for Beam R1F. The second-story beams exhibited negative K_r values of −1.71 kN/mm for Beam L2F and −1.55 kN/mm for Beam R2F.

The proposed thermal analogy approach was then applied to estimate the axial restraint stiffness K_r within the examined frame. Fig. 9 presents the restraint-induced beam axial forces obtained from the linear elastic thermal analysis, in which the axial forces generated by beam elongation at each story can be decomposed to elucidate the mechanisms governing the development of restraint-induced axial response. The results indicate that beam elongation at a given story is primarily restrained by the adjacent stories. Elongation of the first-story beams is restrained by the fixed column bases and the second-story beams (Fig. 9a), whereas elongation of the second-story beams is governed predominantly by the restraint provided by the first-story beams (Fig. 9b), with the contribution from the column bases being relatively minor. Owing to comparable elongations between the first- and second-story beams, deformation compatibility led to partial counteraction of the mutual restraint effects, thereby limiting the effective axial restraint. Consequently, as shown in Fig. 9c, the first-story beams developed significant axial compression, with the restraint dominated by the fixed column bases, while the axial force in the second-story beams was substantially reduced and even transitioned into slight axial tension. This behavior is consistent with the trends observed in the cyclic analysis.

Fig. 10 further compares the deformation pattern predicted by the thermal analogy approach with that obtained from cyclic analysis. The figure also annotates the estimated K_r values, with the values in parentheses indicating the relative errors with respect to the numerical results. The proposed approach successfully reproduced the elongation-induced deformation pattern without requiring nonlinear analysis. Specifically, elongation in the first-story beams generated additional lateral displacements in the columns, while the second-story beams provided restraint to this elongation. The first-story beams exhibited positive K_r values, with relative errors of

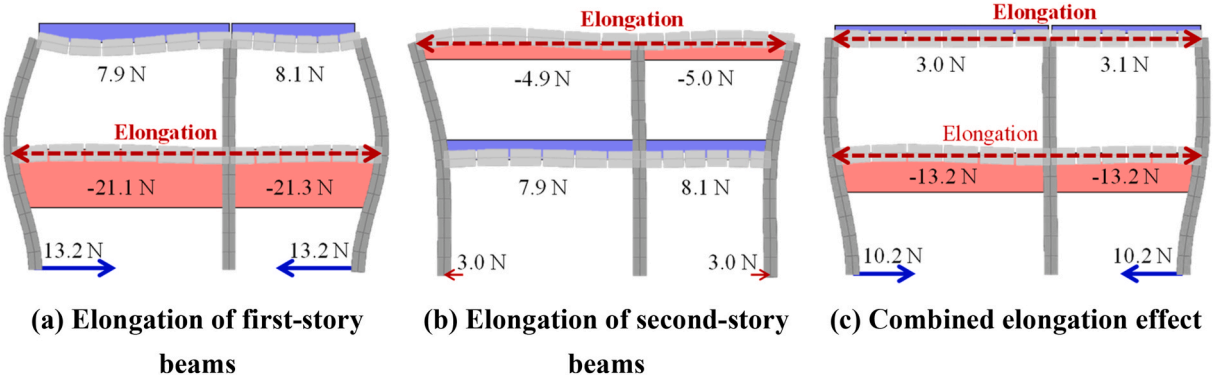


Fig. 9. Axial force diagrams induced by beam elongation under thermal analogy analysis.

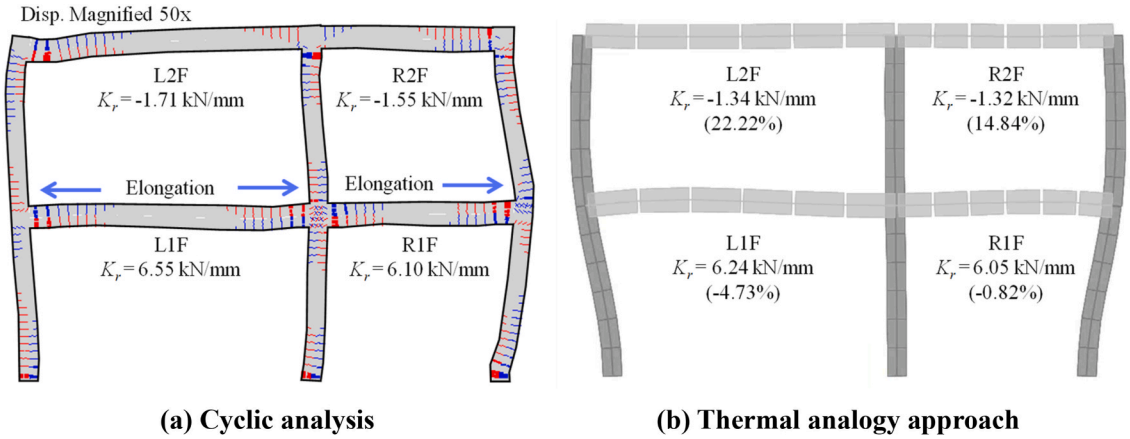


Fig. 10. Comparison of deformation patterns and estimates of axial restraint stiffness.

−4.73% for Beam L1F and −0.82% for Beam R1F, whereas the second-story beams exhibit negative K_r, consistent with the cyclic analysis results. These findings confirm the reliability and the practical applicability of the thermal analogy approach for estimating the beam axial restraint stiffness in RC frame structures.

2.6. *Restraint stiffness degradation*

As illustrated in Fig. 8, axial restraint stiffness progressively degraded throughout the elongation process. To isolate and evaluate the influence of this degradation, a comparative isolated beam model was developed in OpenSees [36] and used as a reference to simulate the elongation restraint effect under stable restraint conditions, as shown in Fig. 11. In this model, the beam was discretized using the same mesh configuration as that adopted in the frame model. A stable axial restraint was provided by connecting an elastic truss element across the beam ends along the longitudinal axis. The left end of the beam was fully fixed, while the right end was coupled through translational degrees of freedom to an auxiliary node, which was rotationally constrained. This isolated-beam model has been experimentally validated in previous studies by the authors [45], where it was shown to reliably reproduce the restraint effects associated with beam hysteretic elongation under a stable restraint.

Fig. 12 compares the damage patterns under both degrading and stable restrained conditions. The cracking patterns under stable restraint (Fig. 12b) validated the boundary conditions in Fig. 11 for simulating double-curvature flexural behavior. Compared to the degrading restraint condition, stable restraint suppressed flexural crack propagation and led to concrete crushing at the beam ends. This behavior is attributed to the further development of axial compression enabled by the stable restraint.

Fig. 13 compares the beam hysteretic response under both restrained conditions. For the stable restraint, the restraint-induced axial compression reached peak values of 36.6 kN and 31.6 kN in Beams L1F and R1F, respectively. However, when the restraint stiffness degradation was accounted for, the axial compression decreased significantly by 68.9% and 66.2%, respectively, resulting in a notable reduction in beam flexural strength. Therefore, neglecting restraint stiffness degradation leads to an overestimation of beam overstrength, potentially resulting in excessive reinforcement optimization and increasing beam vulnerability.

Although restraint stiffness degradation limits the development of the beam axial compression, the compression still exhibits a significant influence on the force demands for adjacent components. The bar charts in Fig. 14 show the composition of shear forces in the first-story columns and joints. The restraint-induced axial compression accounted for 73.5% and 69.6% of the total shear forces in the left and right exterior columns, respectively, and 47.7% and 45.9% in the left and right exterior joints. These findings underscore the necessity of incorporating the restraint-induced axial compression into the seismic design of RC frames. However, the estimation of such compression must account for its limited development under restraint stiffness degradation.

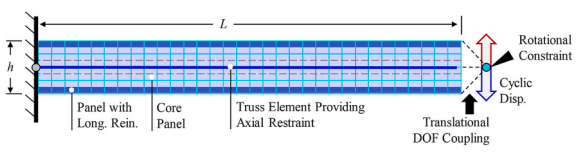


Fig. 11. Isolated model for simulating elongation restraint effects under stable restrained conditions.

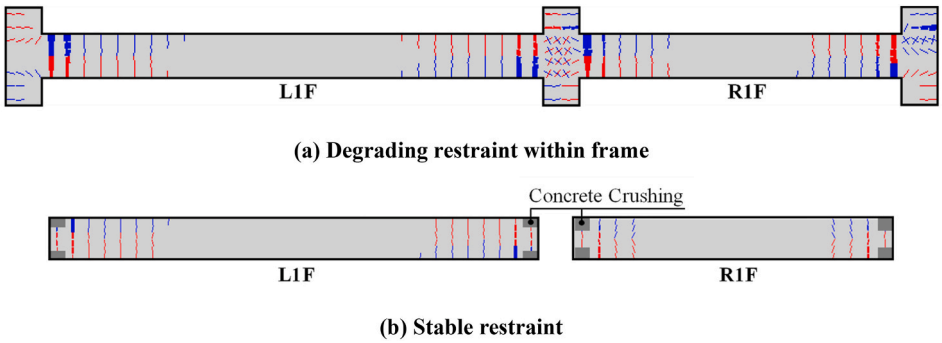


Fig. 12. Comparison of damage patterns under both degrading and stable restrained conditions.

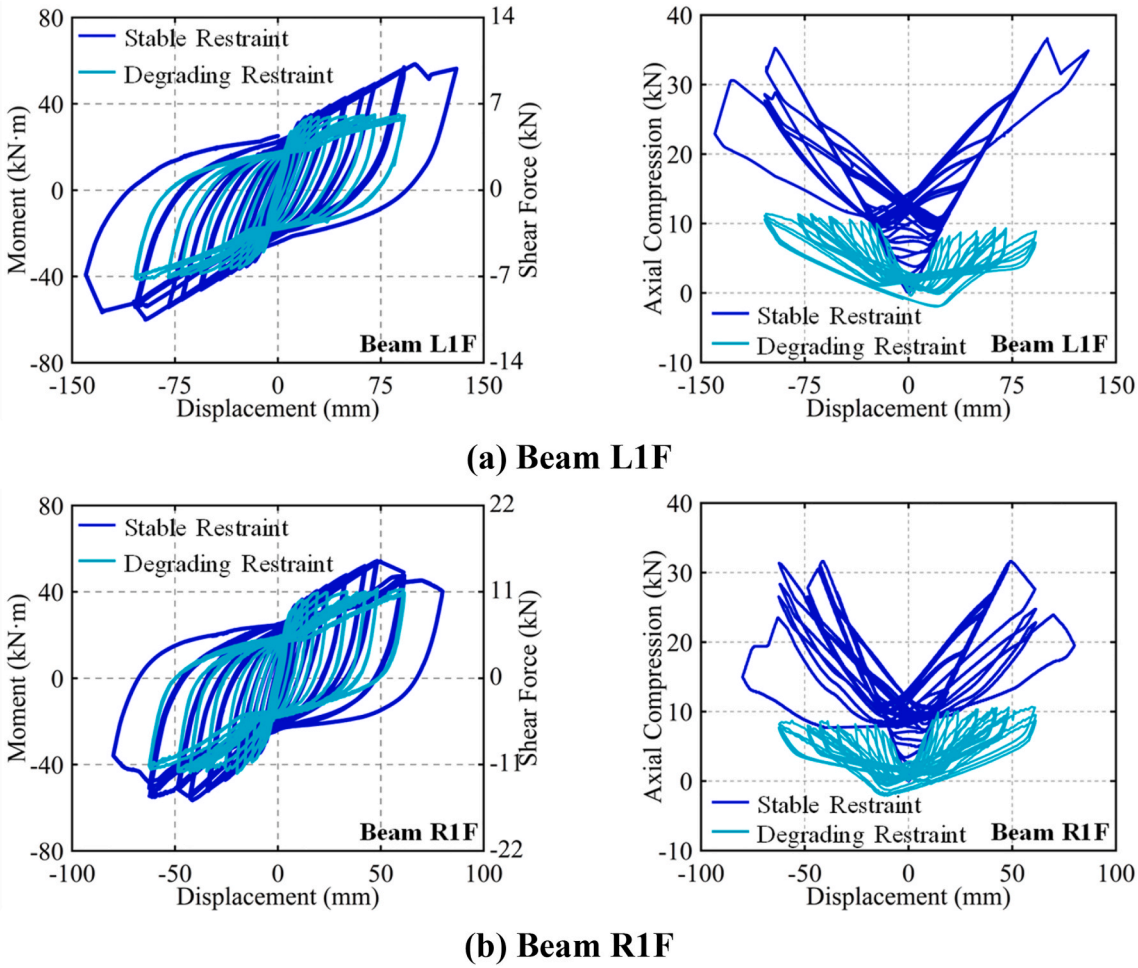


Fig. 13. Comparison of beam hysteretic responses under stable and degrading restrained conditions.

3. Prediction model for restraint-induced beam axial compression

3.1. Mechanical behavior of restrained beams

Fig. 15a compares the hysteretic response and skeleton curves of lateral resistance for Beam R1F from the RC frame in Section 2.3, under both unrestrained and stable restrained conditions. Under stable restraint, the skeleton curve comprises three stages: essential elastic, hardening, and degradation. The transition from elastic to hardening corresponds to the yielding of longitudinal reinforcement,

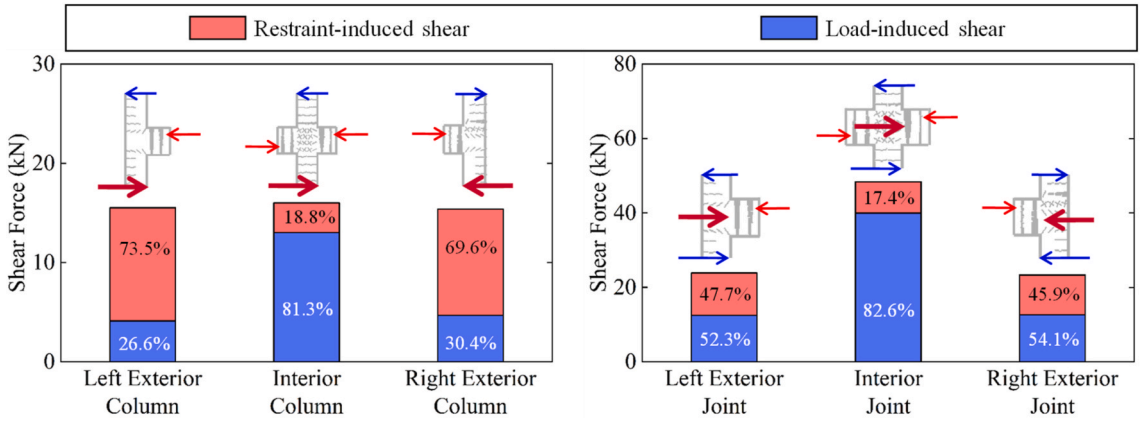


Fig. 14. Shear force composition in columns and joint under restraint effects.

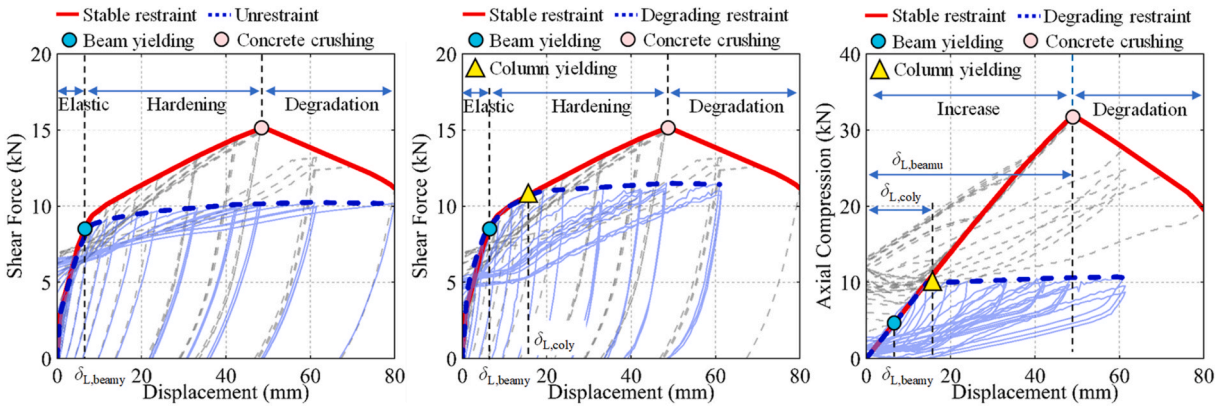


Fig. 15. Hysteretic responses of Beam R1F under different restrained conditions.

while the onset of concrete crushing marks the initiation of strength degradation. Compared to the unrestrained condition, the elongation restraint induces pronounced post-yield hardening. This behavior is attributed to the development of restraint-induced axial compression, which enhances the beam flexural strength. In this case, the hardening ratio, defined as the ratio of hardening stiffness to elastic stiffness, reached 0.127, resulting in a 47.5% increase in peak lateral resistance compared to the unrestrained condition.

Fig. 15b depicts the hysteretic response and skeleton curve for Beam R1F under degrading restrained condition, reflecting the restraint behavior within the frame system. While a hardening trend remains evident after beam yielding, the onset of column yielding leads to a notable reduction in the hardening ratio, resulting in a less pronounced overstrength compared to that under stable restraint. This reduction is primarily attributed to the restraint stiffness degradation, which limits further development of restraint-induced axial compression.

Fig. 15c illustrates the evolution of restraint-induced axial compression with lateral displacement under both restrained conditions. Under stable restraint, the axial compression increases approximately linearly until concrete crushing occurs. In contrast, under degrading restraint, the axial compression initially follows a similar development but becomes markedly limited after column yielding, as the associated reduction in column lateral stiffness leads to a progressive loss of effective axial restraint. Similar response characteristics have been reported in experimental frame subassembly tests [20], where column yielding was observed to inhibit further development of beam axial compression. These observations indicate that the axial compression corresponding to column yielding represents a more realistic upper bound under degrading restraint conditions. Accordingly, for seismic design, it is therefore essential to adopt the axial compression corresponding to column yielding, rather than the peak value attained under idealized stable restraint, to avoid substantial overestimation.

To incorporate the restraint degradation effect while maintaining applicability in design, a normalized parameter termed the

effective restraint ductility (ERD) is introduced herein. ERD characterizes the deformation capacity of the beam prior to column yielding and is defined as:

$$\mathrm{ERD} = \delta_{\mathrm{L,coly}} / \delta_{\mathrm{L,beamy}} \tag{4}$$

Where $\delta_{\mathrm{L,beamy}}$ and $\delta_{\mathrm{L,coly}}$ represent the lateral displacements corresponding to beam yielding and column yielding, respectively. In addition, the ultimate restraint ductility (URD) is defined to represent the deformation capacity of the beam prior to the degradation of axial compression under stable restraint conditions:

$$\mathrm{URD} = \delta_{\mathrm{L,beamu}} / \delta_{\mathrm{L,beamy}} \tag{5}$$

Where $\delta_{\mathrm{L,beamu}}$ corresponds to the lateral displacement at which the axial compression reaches its maximum value under stable restraint conditions.

Since the development of axial compression prior to column yielding follows a similar and approximately linear growth trend for both stable and degrading restraint conditions, the axial compression under degrading restraint can be estimated from the stable restraint results using the corresponding ERD value. Therefore, the remainder of this section develops a prediction model for estimating restraint-induced beam axial compression as a function of ERD. This model is calibrated through regression of detailed numerical simulations of beam hysteretic responses under stable restrained conditions. The determination of ERD for seismic design is subsequently discussed in Section 4.2.

Table 1
Beam parameters for parametric assessment.

Group	SubGroup	Specimen	*b*(mm)	*h*(mm)	*h/b*	L_t(mm)	λ	ρ_l(%)	ρ_{sv}(%)	f_c(MPa)
G_{ref}		*Gref*-05	**400**	**800**	**2.0**	**6400**	**4**	**0.5**	**1.00**	**20**
(reference model)		*Gref*-10	**400**	**800**	**2.0**	**6400**	**4**	**1.0**	**1.00**	**20**
		Gref-15	**400**	**800**	**2.0**	**6400**	**4**	**1.5**	**1.00**	**20**
		Gref-20	**400**	**800**	**2.0**	**6400**	**4**	**2.0**	**1.00**	**20**
G*h*	G*h*-500	G*h*-500-05	250	**500**	2.0	4000	4	**0.5**	1.00	20
		G*h*-500-10	250	**500**	2.0	4000	4	**1.0**	1.00	20
		G*h*-500-15	250	**500**	2.0	4000	4	**1.5**	1.00	20
		G*h*-500-20	250	**500**	2.0	4000	4	**2.0**	1.00	20
	G*h*-1000	G*h*-1000-05	500	**1000**	2.0	8000	4	**0.5**	1.00	20
		G*h*-1000-10	500	**1000**	2.0	8000	4	**1.0**	1.00	20
		G*h*-1000-15	500	**1000**	2.0	8000	4	**1.5**	1.00	20
		G*h*-1000-20	500	**1000**	2.0	8000	4	**2.0**	1.00	20
Gλ	Gλ-2	Gλ-2-05	400	800	2.0	**3200**	**2**	**0.5**	1.00	20
		Gλ-2-10	400	800	2.0	**3200**	**2**	**1.0**	1.00	20
		Gλ-2-15	400	800	2.0	**3200**	**2**	**1.5**	1.00	20
		Gλ-2-20	400	800	2.0	**3200**	**2**	**2.0**	1.00	20
	Gλ-6	Gλ-6-05	400	800	2.0	**9600**	**6**	**0.5**	1.00	20
		Gλ-6-10	400	800	2.0	**9600**	**6**	**1.0**	1.00	20
		Gλ-6-15	400	800	2.0	**9600**	**6**	**1.5**	1.00	20
		Gλ-6-20	400	800	2.0	**9600**	**6**	**2.0**	1.00	20
G*b*	G*b*-4	G*b*-4-05	**200**	800	**4.0**	6400	2	**0.5**	1.00	20
		G*b*-4-10	**200**	800	**4.0**	6400	2	**1.0**	1.00	20
		G*b*-4-15	**200**	800	**4.0**	6400	2	**1.5**	1.00	20
		G*b*-4-20	**200**	800	**4.0**	6400	2	**2.0**	1.00	20
	G*b*-1.3	G*b*-1.3-05	**600**	800	**1.3**	6400	2	**0.5**	1.00	20
		G*b*-1.3-10	**600**	800	**1.3**	6400	2	**1.0**	1.00	20
		G*b*-1.3-15	**600**	800	**1.3**	6400	2	**1.5**	1.00	20
		G*b*-1.3-20	**600**	800	**1.3**	6400	2	**2.0**	1.00	20
Gf_c	Gf_c-25	Gf_c-25-05	400	800	2.0	6400	4	**0.5**	1.00	**25**
		Gf_c-25-10	400	800	2.0	6400	4	**1.0**	1.00	**25**
		Gf_c-25-15	400	800	2.0	6400	4	**1.5**	1.00	**25**
		Gf_c-25-20	400	800	2.0	6400	4	**2.0**	1.00	**25**
	Gf_c-30	Gf_c-30-05	400	800	2.0	6400	4	**0.5**	1.00	**30**
		Gf_c-30-10	400	800	2.0	6400	4	**1.0**	1.00	**30**
		Gf_c-30-15	400	800	2.0	6400	4	**1.5**	1.00	**30**
		Gf_c-30-20	400	800	2.0	6400	4	**2.0**	1.00	**30**
Gρ_{sv}	Gρ_{sv}-50	Gρ_{sv}-50-05	400	800	2.0	6400	4	**0.5**	**0.50**	20
		Gρ_{sv}-50-10	400	800	2.0	6400	4	**1.0**	**0.50**	20
		Gρ_{sv}-50-15	400	800	2.0	6400	4	**1.5**	**0.50**	20
Gρ_{sv}	Gρ_{sv}-25	Gρ_{sv}-25-05	400	800	2.0	6400	4	**0.5**	**0.25**	20
		Gρ_{sv}-25-10	400	800	2.0	6400	4	**1.0**	**0.25**	20
		Gρ_{sv}-25-15	400	800	2.0	6400	4	**1.5**	**0.25**	20

3.2. Parametric database for prediction model development

To generate detailed results, a total of 42 RC beams were considered, with their parameters given in Table 1. The parameters examined include the section height h and width b, span-to-depth ratio L/h, sectional single-sided longitudinal reinforcement ratio ρ_l, concrete compressive strength f_c, and transverse reinforcement ratio ρ_{sv}. All members utilized HRB400 steel for both longitudinal and transverse reinforcement, with a yield strength (f_y, f_{yv}) of 400 MPa.

The axial restraint level is characterized by the restraint coefficient, defined as:

$$\kappa = K_r/K_a \tag{6}$$

Where K_r is the imposed axial restraint stiffness, and K_a denotes beam axial stiffness, given by:

$$K_a = E_c bh/L \tag{7}$$

Where E_c is the concrete elastic modulus, taken as 30 GPa, 32.0 GPa, and 33.5 GPa for f_c of 20 MPa, 25 MPa, and 30 MPa, respectively, in accordance with standards [24]. Each beam was analyzed under eight restraint levels: $\kappa = 0.0$ (unrestrained), 0.05, 0.1, 0.2, 0.4, 0.6, 0.8, and 1.0, resulting in a total of 336 cyclic simulations.

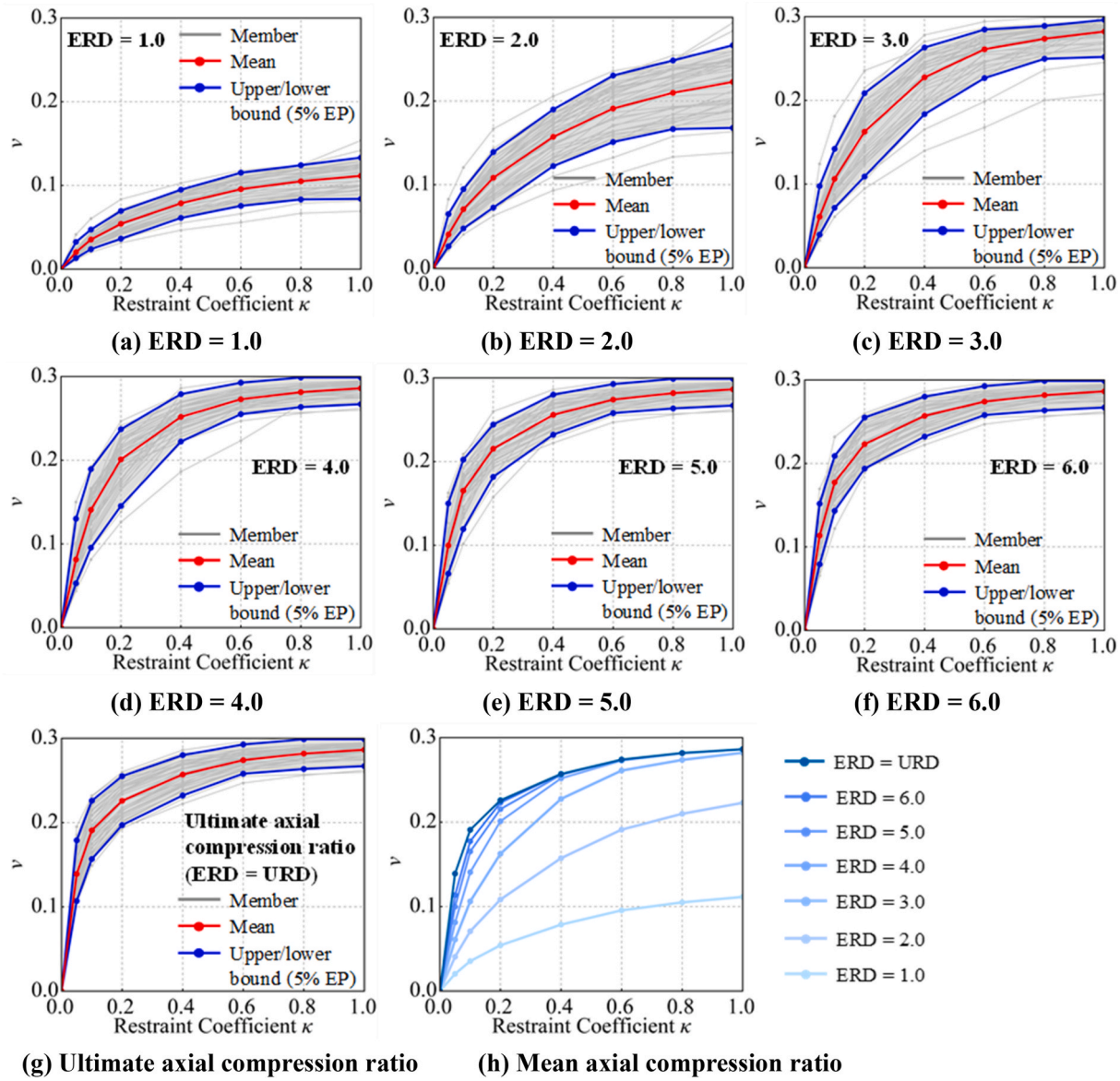


Fig. 16. Variation of axial compression ratio ν with restraint coefficient κ under different ERD values.

The isolated beam model presented in Fig. 11 was adopted to simulate the hysteretic response of beams under double-curvature loading, representative of deformation patterns in frame structures. In each analysis, lateral cyclic loading was applied incrementally with a single-cycle drift step of 0.001 rad until the longitudinal reinforcement yielded. The corresponding yield drift was then adopted as the increment for subsequent loading levels, with three cycles applied at each level. Loading was continued until degradation was observed in lateral strength, beam elongation, and axial compression responses.

3.3. Restraint-induced axial compression levels

To quantify the restraint-induced axial compression level, the ultimate axial compression ratio is introduced and defined as:

$$\nu_{ult} = N_{\max} / f_c bh \tag{8}$$

Where $N_{\max}$ denotes the maximum axial compression achievable under stable restraint conditions.

As illustrated in Fig. 15c, the development of axial compression prior to column yielding remains nearly identical for stable and degrading restraint conditions. Accordingly, the axial compression ratio under degrading restraint can be estimated by scaling the ultimate value ν_{ult} using ERD, expressed as:

$$\nu = \min\left(\frac{ERD}{URD} \cdot \nu_{ult}, \nu_{ult}\right) \tag{9}$$

when ERD ≥ URD, the axial compression fully develops and reaches the ultimate value as that under stable restraint conditions.

Fig. 16 illustrates the variation of ν with the restraint coefficient κ across the examined members under different ERD values. For reference, the corresponding ultimate value ν_{ult} is also plotted. In these figures, the red curves denote the mean trend, while the blue curves represent the upper and lower bounds associated with a 5% exceedance probability.

The results indicate that ν increased with κ, exhibiting a diminishing growth rate as κ increases. With larger ERD values, the ν-κ curve became increasingly convex, indicating a more rapid development of axial compression at low restraint levels. At a given κ, higher ERD values led to larger ν values, which gradually approached ν_{ult}. As shown in Fig. 16h, when ERD reached 6, the ν-κ curve aligned well with the ν_{ult}-κ curve, indicating that restraint-induced axial compression was nearly fully developed under such conditions.

3.4. Statistical representation of ν-κ relationship

To represent the nonlinear relationship between the axial compression ratio ν and the restraint coefficient κ, a power-based function was introduced:

$$\nu = \nu_{\kappa = 1.0} [1 - (1 - \kappa)^{\beta}] \tag{10}$$

Where $\nu_{\kappa = 1.0}$ denotes ν at κ=1.0, and β is a curvature-controlling exponent. A larger β implies a steeper rise in the ν-κ curve, indicating more rapid axial compression development.

Fig. 17 presents the fitted results of Eq. (10) for two representative members, G*ref*-05 and G*ref*-15, under various ERD values. As ERD increased, ν exhibited more rapid growth. The fitted curves accurately captured this trend, demonstrating the flexibility of the proposed function to model the ν–κ relationship through appropriate calibration of β. Moreover, the consistent increase of β with ERD confirms its sensitivity to ductility demand and demonstrates its suitability for regression analysis based on ERD.

Fig. 18 presents the statistical distribution of the calibrated β and $\nu_{\kappa = 1.0}$ using box plots. Both parameters show a positive correlation with ERD, with β exhibiting a progressively accelerating growth trend with increasing ERD. On the other hand, $\nu_{\kappa = 1.0}$ increased approximately linearly at lower ERD values and subsequently reached a plateau as ERD exceeds 3.0. This plateau-shaped response reflects the attainment of the URD under the condition of $\kappa = 1.0$, beyond which further increases in ERD do not lead to the development of additional axial compression. To capture these trends, exponential and bilinear regression models were adopted for

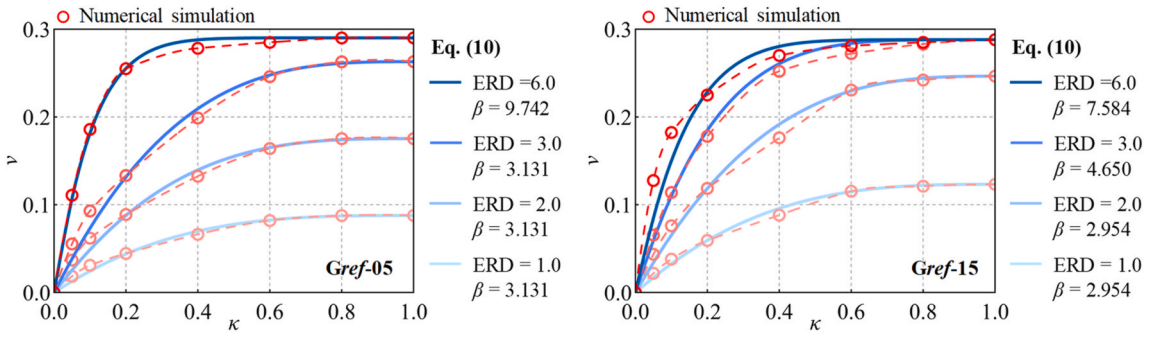


Fig. 17. Fitted μ–κ relationships for representative members under different ERD values.

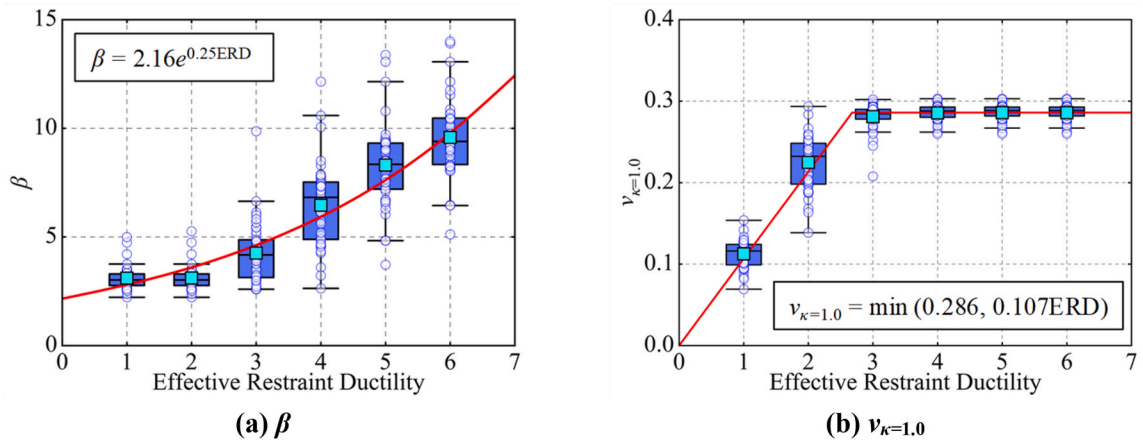


Fig. 18. Statistical distribution of fitted parameters in the v–κ model with their regression trends.

β and $v_{\kappa\,=\,1.0}$ as:

$$\beta = 2.16e^{0.25\mathrm{ERD}} \tag{11}$$

$$v_{\kappa\,=\,1.0} = \min\,(0.286,\ 0.107\mathrm{ERD}) \tag{12}$$

Fig. 19a compares the predicted v values using Eqs. (10)–(12) against the numerical simulation results. The horizontal axis v_{FEA} represents the numerical values, while the vertical axis v_{pred} denotes the model predictions. A ±30% relative error band is shaded for reference. The corresponding distribution of relative errors is shown in Fig. 19b. The results indicate that 80.2% of the predictions fell within ±20% relative error and 90.2% within ±30%, with a coefficient of determination R^2 of 0.941. These confirm the reliability of the proposed ERD-based model in estimating the restraint-induced beam axial compression across a wide range of beam parameters and restraint conditions.

4. Seismic design incorporating beam elongation restraint effects

4.1. Proposed design methodology

Building upon the thermal analogy approach for estimating the beam axial restraint stiffness (Section 2) and the ERD-based prediction model for restraint-induced axial compression (Section 3), a seismic design methodology is established herein for RC frames to explicitly account for beam elongation restraint effects. The methodology consists of four sequential steps on the basis of an initial code-based seismic design, including member geometry, material properties, and reinforcement layout, and is implemented within seismic load combinations. The four steps are summarized as follows.

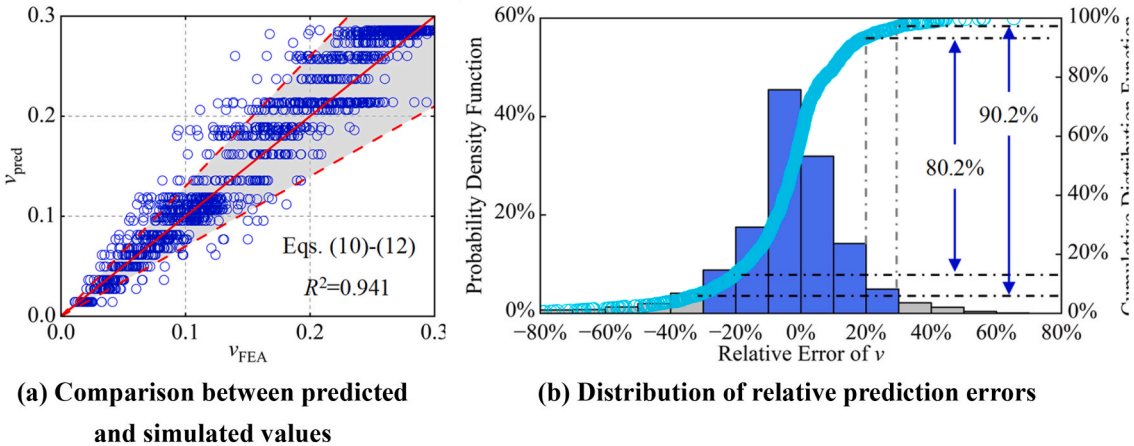


Fig. 19. Validation of ERD-based model for predicting restraint-induced axial compression.

(i) **Evaluation of beam axial restraint stiffness:** The axial restraint stiffness of each beam within the frame is estimated using the proposed thermal analogy approach.

(ii) **Determination of restraint-induced beam axial compression:** Based on the estimated restraint stiffness, the corresponding axial compression is predicted using the ERD-based model developed in this study. The determination of ERD is described in detail in Section 4.2.

(iii) **Beam reinforcement optimization:** To mitigate beam flexural overstrength induced by the estimated axial compression, the longitudinal reinforcement is optimized through axial-moment interaction analysis. The optimization procedure is described in Section 4.3.1.

(iv) **Column and joint strengthening:** Restraint-induced force demands on columns and joints associated with the estimated beam axial compression are evaluated, and the corresponding reinforcement enhancements are implemented to satisfy these demands. If the required column reinforcement exceeds the maximum allowable reinforcement ratio specified in design codes, the column cross-section is increased accordingly, and Steps (i)–(iv) are repeated until reinforcement requirements satisfy codified limits. The procedures for quantifying column and joint demands are presented in Sections 4.3.2 and 4.3.3, respectively.

In practical design applications, the final reinforcement detailing should be governed by the envelope of seismic and non-seismic load combinations and must also satisfy the serviceability limit state requirements prescribed by design codes.

4.2. *Determination of effective restraint ductility (ERD)*

Multi-degree-of-freedom shear models are widely used for simulating the seismic response of multi-story building structures. Among these models, the tri-linear backbone curve [46] has been shown to reliably represent the inter-story behavior of RC frames with acceptable modeling complexity and accuracy [47–49].

Fig. 20 shows the numerical hysteretic response of the first story of the RC frame examined in Section 2.3, along with its idealized tri-linear backbone curve. Prior to yielding, the story exhibits essentially linear behavior, with initial stiffness accounting for the flexural cracking effects in frame members. The yield strength V_y represents the actual lateral resistance considering design redundancies, typically governed by beam flexural yielding. This is consistent with design principles in RC frames, where beams are expected to yield prior to columns to ensure favorable energy dissipation mechanisms. Accordingly, the yield displacement δ_y corresponds to the beam yielding displacement $\delta_{L,beamy}$.

Between the yield and ultimate points, the backbone curve transitions from an elastic to a plastic response. The ultimate strength V_u corresponds to the fully developed lateral resistance of the story, generally attained after column yielding and accompanied by reinforcement hardening. Beyond the ultimate displacement δ_u, the structure is assumed to maintain deformation capacity without further increase in lateral resistance.

Although guidelines have been proposed [46] for defining the backbone curve parameters, the ultimate point typically corresponds to a structural state involving notable column damage. Thus, the column yielding displacement $\delta_{L,coly}$, used in the definition of ERD in Eq. (4), lies between δ_y and δ_u. Based on the backbone curves of the examined frame and previous studies, it is observed that although stiffness degradation occurs after beam yielding, the lateral stiffness prior to column yielding remains considerably greater than the stiffness between the yield to ultimate points. Accordingly, to facilitate the evaluation, the column yielding displacement is approximated by extending the pre-yield stiffness up to V_u. The corresponding lateral displacement is taken as $\delta_{L,coly}$. Using this assumption, ERD can be estimated by the overstrength factor, defined as:

$$\text{ERD} \approx \Omega_u = V_u / V_y \tag{13}$$

With reference to Fig. 20, the measured displacements $\delta_{L,beamy}$ and $\delta_{L,coly}$ were 3.05 mm and 6.78 mm, respectively, corresponding to story drift ratios of 0.21% and 0.47%. From Eq. (4), the resulting ERD is computed as 2.22. Alternatively, using the measured values of $V_y = 16.8$ kN and $V_u = 34.1$ kN, the ERD calculated from Eq. (13) is 2.03. This slight underestimation is attributed to the assumption of

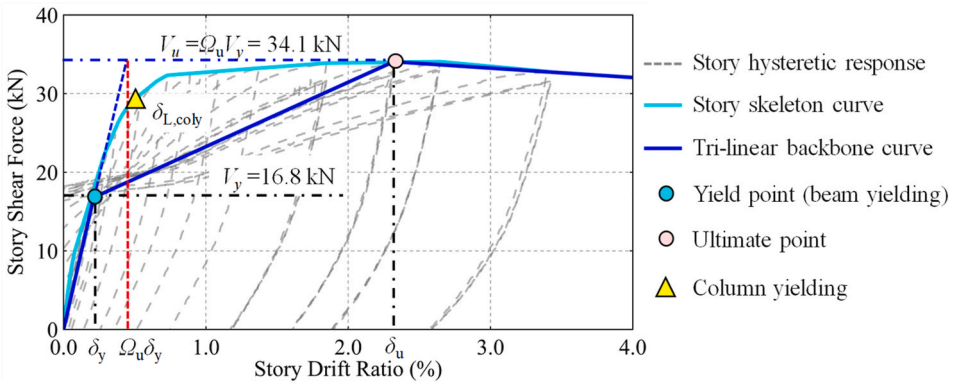


Fig. 20. Hysteretic response and idealized tri-linear backbone curve of the story resistance.

maintaining the initial stiffness beyond the yield point. Nevertheless, the close agreement confirms the applicability of using the Ω_u as a surrogate for ERD, especially given the availability of extensive Ω_u datasets in the literature.

A value of 3.0 is typically recommended [46] for Ω_u for RC frames in US provisions. However, this value may not be directly applicable to RC frames designed under other national codes, which may differ in structural detailing, load combination schemes, and ductility requirements. To account for such differences, Fig. 21 presents the statistical distribution of ERD values inferred from Ω_u datasets derived from 134 numerical simulations of RC frames designed according to the Chinese seismic code [50], covering intensity levels from 7 to 9.

The ERD data were fitted using a lognormal distribution, and the corresponding cumulative distribution function (CDF) is expressed as:

$$P(\mathrm{ERD} \le d) = \Phi\left(\frac{\ln d - \ln 2.27}{0.24}\right) \tag{14}$$

where $\Phi(\cdot)$ denotes the cumulative distribution function of the standard normal distribution.

In this study, two distinct values of ERD were adopted to address different design objectives. An ERD of 1.77, corresponding to the 15% reliability level shown in Fig. 21, was adopted for beam reinforcement optimization. This conservative value helps prevent over-reduction in reinforcement, which could otherwise hinder the beams from achieving the intended flexural strength under design-level seismic loading. On the other hand, an ERD of 2.91, corresponding to the 85% reliability level, was employed to estimate the additional seismic force demands on columns and joints induced by beam axial compression, thus providing a safety margin in seismic design.

4.3. Design of different components

4.3.1. Beam reinforcement optimization

To mitigate the induced flexural overstrength, the axial restraint stiffness K_r acting on the beam is first estimated using the proposed thermal analogy method. This stiffness is then used to calculate the restraint coefficient κ using Eqs. (6) and (7). Based on the computed κ and an ERD at a specified reliability level, the corresponding axial compression ratio v is evaluated using the prediction model defined by Eqs. (10)–(12). Finally, the longitudinal reinforcement ratio, initially determined by seismic design codes, is subsequently optimized using the axial-moment interaction relationship informed by the estimated axial compression ratio μ, thereby mitigating the overstrength effect.

4.3.2. Restraint-induced column force demands

The restraint-induced beam axial compression imposes additional shear forces on adjacent columns. As demonstrated in Section 2.5, beams located at upper stories may experience axial tension, which can partially offset the column shear forces. However, due to the limited tensile capacity of RC members, the influence of axial tension is generally negligible compared to axial compression. Consequently, the beam axial tension is conservatively disregarded, and the restraint-induced column shear force in the j-th story can be calculated as:

$$\Delta \mathrm{V}_{\mathrm{c},j} = \left| \sum_{i=j}^{n} \left(N_l^i - N_r^i \right) \right| \tag{15}$$

where n is the total number of stories, and N_l^i and N_r^i represents the axial compression in the left and right beams at the i-th story, respectively.

The shear amplification coefficient η_v for columns is expressed as:

$$\eta_v = \left(\Delta \mathrm{V}_c + V_c^{\mathrm{code}} \right) / V_c^{\mathrm{code}} \tag{16}$$

where V_c^{code} denotes the column shear demand specified by seismic design codes, incorporating relevant amplification factors [51],

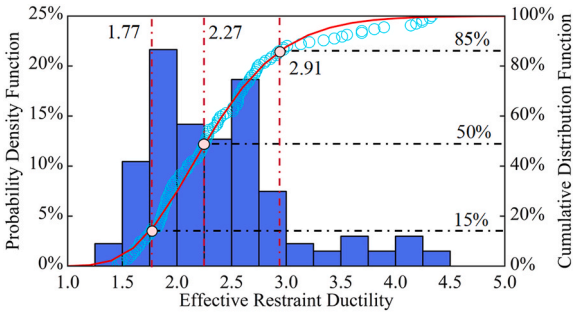


Fig. 21. Statistical distribution of ERD inferred from overstrength ratios of RC frames.

such as the internal force amplification for the base of the first-story columns.

The amplified column-end moment demand induced by beam axial compression is then proportionally scaled as:

$$M_c = \eta_v M_c^{\text{code}} \tag{17}$$

where M_c^{code} is the column-end moment demand determined from code-based design.

Furthermore, the beam overstrength resulting from axial compression must be considered in column design. The total column-end moment demands at a joint should satisfy the following equilibrium condition:

$$\Sigma M_{\text{c}} = \eta_{\text{c}} \Sigma M_{\text{b}} \tag{18}$$

Where ΣM_{c} is the total column-end moment demand at the joint, ΣM_{b} is the total beam-end moment strength at the joint, accounting for the overstrength induced by axial compression, and η_{c} is the moment amplification coefficient, taken as 1.2 according to the code provisions [51] when ΣM_{b} is calculated based on the as-built reinforcement.

If Eq. (15) is not satisfied, the column-end moment demands should be proportionally adjusted to ensure beam yielding precedes column yielding, thereby preserving the intended strong-column/weak-beam yield mechanism. Column reinforcement design should then be conducted based on the adjusted moment demands.

4.3.3. *Restraint-induced joint shear demands*

Fig. 22 depicts the force transfer mechanisms within a beam-column joint, with and without consideration of beam axial compression effects. In the absence of axial compression, the joint shear demand is calculated as:

$$\text{V}_j = \eta_j \cdot \max\left(T_{u,l} + C_{s,r} + C_{c,r} - V_{c,u}^{l}, T_{u,r} + C_{s,l} + C_{c,l} - V_{c,u}^{r}\right) \tag{19}$$

where η_{j} is the shear amplification coefficient determined by the seismic design level following the standards [51]. $C_{\text{s,r}}$ and $C_{\text{c,r}}$ represent the compressive forces in the reinforcement and concrete of the right beam end, respectively, while $C_{\text{s,l}}$ and $C_{\text{c,l}}$ represent those of the left beam end. $T_{\text{u,l}}$ and $T_{\text{u,r}}$ denote the tensile forces in the top longitudinal reinforcement of the left and right beams, respectively. $V_{c,u}^{l}$ and $V_{c,u}^{r}$ are the corresponding shear forces in the upper columns.

Based on cross-sectional equilibrium, the tensile forces in the bottom longitudinal reinforcement can be expressed as $T_{\text{l,r}} = C_{\text{s,l}} + C_{\text{c,l}}$ and $T_{\text{d,r}} = C_{\text{s,r}} + C_{\text{c,r}}$. Substituting into Eq. (19), the shear demand can be rewritten as:

$$\text{V}_j = \eta_j \cdot \max\left(T_{u,l} + T_{d,r} - V_{c,u}^{l}, T_{u,r} + T_{l,r} - V_{c,u}^{r}\right) \tag{20}$$

When beam axial compression is considered, it is transmitted through the compression zones at the beam ends, resulting in an adjusted joint shear demand:

$$\text{V}_j = \eta_j \cdot \max\left(T_{u,l} + T_{d,r} + N_r - V_{c,u}^{l}, T_{u,r} + T_{l,r} + N_l - V_{c,u}^{r}\right) \tag{21}$$

where N_{l} and N_{r} are the restraint-induced axial compression in the left and right beams, respectively. As shown, the beam axial compression increases the joint shear demand and should therefore be considered in the joint design. Conversely, although axial tension in the beams at the upper stories may reduce the joint shear, its effect is insignificant due to the limited tensile capacity of RC members and is therefore conservatively disregarded.

5. Application and validation studies

In this section, the proposed seismic design methodology is applied to a prototype RC frame structure. Comparisons are also carried out against detailed numerical simulations in order to illustrate the effectiveness of the proposed design methodology in accounting for

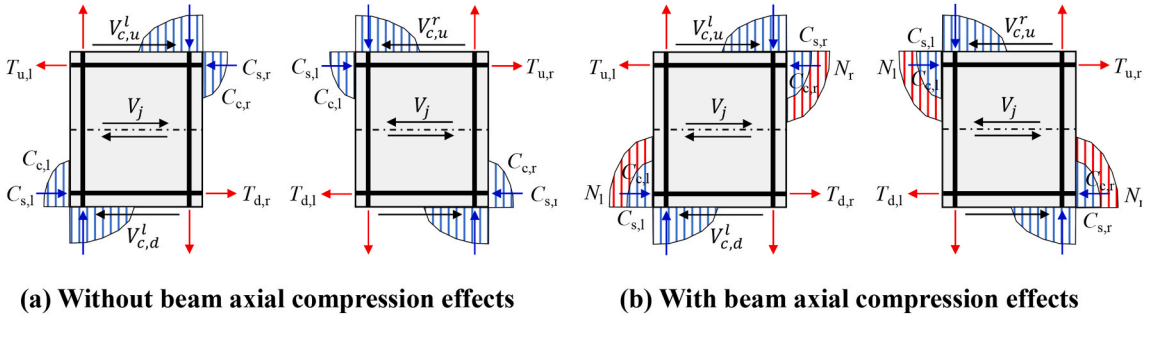


Fig. 22. Force transfer mechanisms within a beam-column joint.

beam elongation restraint effects under cyclic loading.

5.1. Prototype RC frame structure

The prototype structure, illustrated in Fig. 23, is a three-story, four-bay RC frame with uniform bay lengths of 4.0 m. The first story is 4.0 m high, while the second and third stories each have a height of 3.0 m, resulting in a total height of 10.0 m. The frame was designed in accordance with design codes [24,51] to resist both gravity and seismic loads.

The gravity loads consisted of self-weight, along with uniformly distributed dead and live loads of 2.0 kN/m^2. The seismic Intensity 9 [51], corresponding to a design ground acceleration of 0.4g, was considered. All columns had a cross-section of 600 mm × 600 mm, and beams were 200 mm × 500 mm. The concrete grade was C30 ($f_c = 20$ MPa), and HRB400 steel was used for both longitudinal and transverse reinforcement ($f_y = f_{yv} = 400$ MPa).

The central lateral frame was selected for applying the design methodology and subsequent numerical evaluations. Reinforcement details based on design codes are shown in Fig. 23. The sectional single-sided longitudinal reinforcement ratios ρ_l of the first-, second-, and third-story beams are 0.95%, 0.95%, and 0.60%, respectively. The first-, second-, and third-story columns have total longitudinal reinforcement ratios ρ_{tot} of 1.63%, 1.05%, and 1.05%, respectively, with a consistent volume of transverse reinforcement ratio ρ_v of 1.05% across all stories.

5.2. Implementation of proposed design methodology

5.2.1. Evaluation of beam axial restraint stiffness

Fig. 24 presents the restraint-induced beam axial forces obtained using the proposed thermal analogy approach, in which the axial forces generated by beam elongation at each story are decomposed. The results indicate that beam elongation at a given story is primarily restrained by adjacent stories. The first-story beams developed significant axial compression, primarily due to the restraint provided by the fixed column bases. In contrast, owing to comparable elongations between adjacent stories and deformation compatibility, beams at higher stories exhibit substantially reduced axial forces and may even develop slight axial tension. This behavior is consistent with the analysis results of the test frame discussed in Section 2.5 and previously illustrated in Fig. 9.

Fig. 25 further illustrates the deformation pattern induced by beam elongation and the corresponding axial restraint stiffness K_r, estimated using the thermal analogy approach. The first-story beams were subjected to axial compression with positive K_r values. Owing to their more confined location within the frame, the interior beams developed higher restraint stiffness than the exterior beams, with an increase of 56.3%. In contrast, the second- and third-story beams experienced axial tension, thereby providing additional restraint to the first-story beams. However, their combined restraining effect accounted for less than 15% of the total restraint stiffness of the first-story beams. Accordingly, and in accordance with the discussion in Section 4.3, the beam reinforcement optimization and the associated column and joint strengthening were applied solely at the first story, where restraint-induced axial compression was exclusively present.

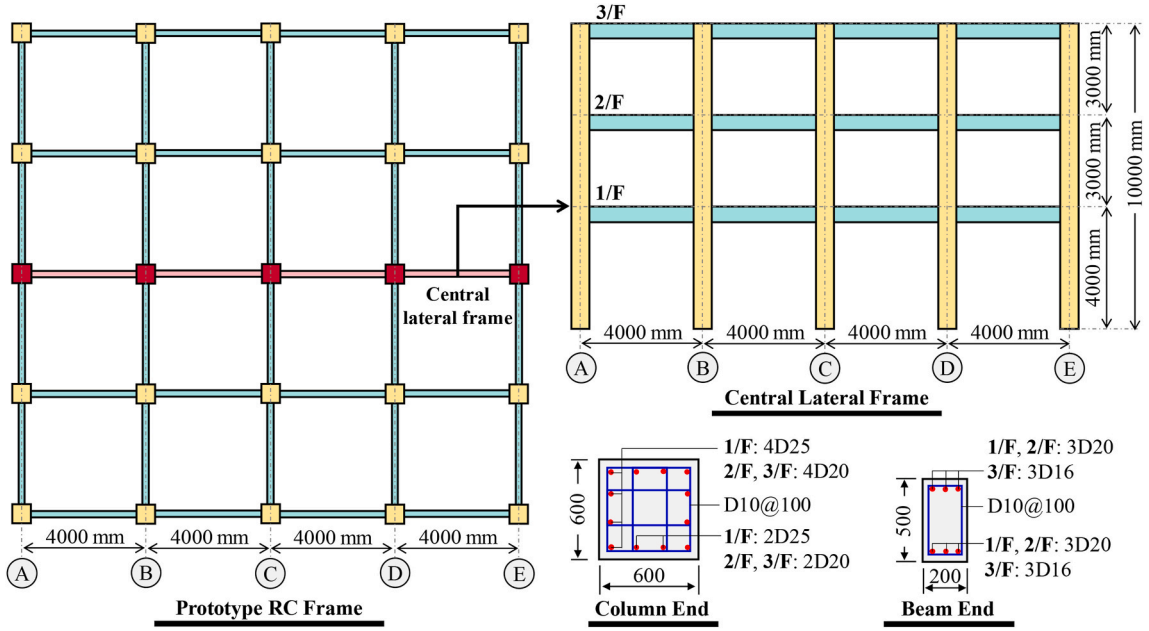


Fig. 23. Configuration and reinforcement details of the prototype three-story four-bay RC frame.

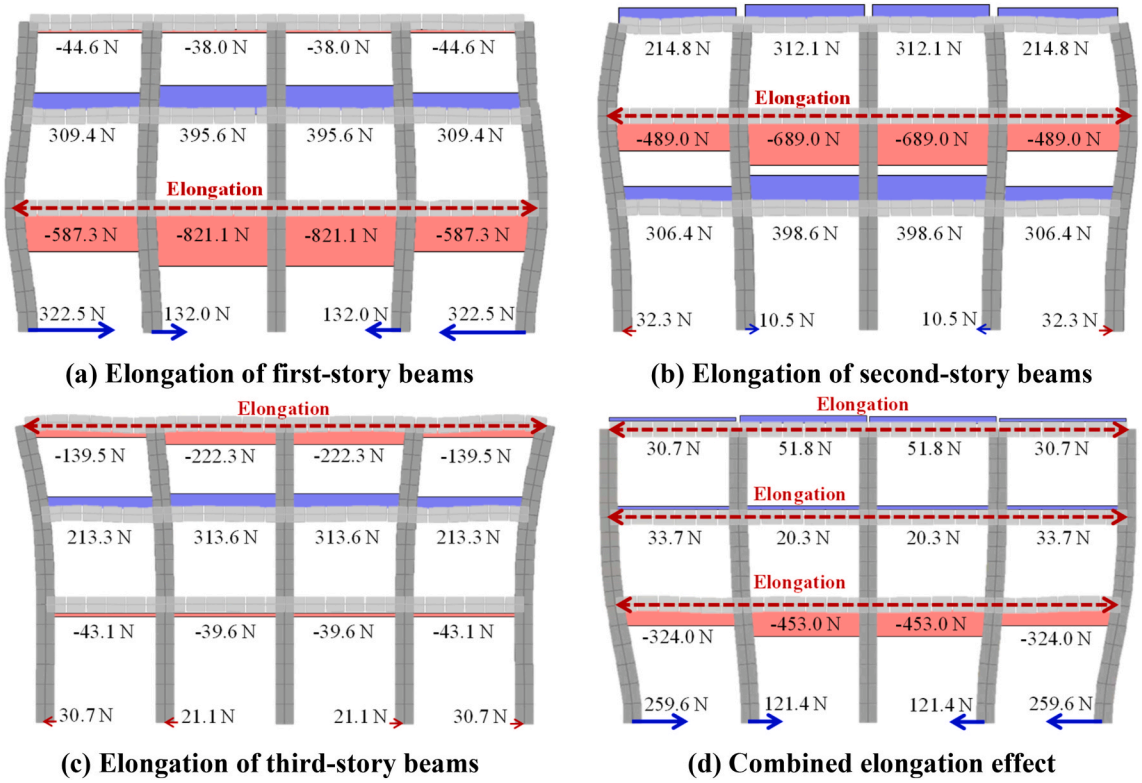


Fig. 24. Axial force diagrams induced by beam elongation under thermal analogy analysis.

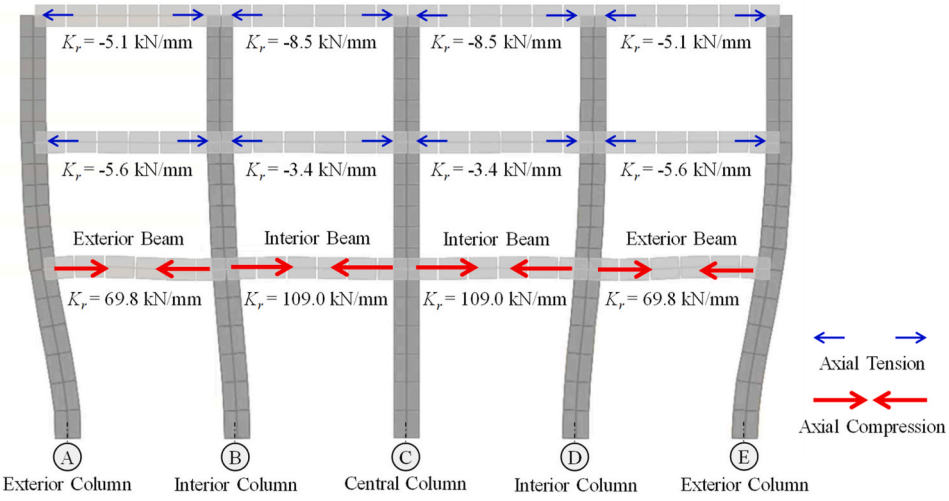


Fig. 25. Deformation pattern and estimated K_r of prototype frame using thermal analogy approach.

5.2.2. Determination of restraint-induced beam axial compression

The restraint coefficients κ for the first-story beam were computed using Eqs. (6) and (7), based on the estimated K_r values. The corresponding axial compression ratios ν were then estimated using the prediction model in Eqs. (10)–(12), as a function of κ and an ERD at specified reliability levels.

For 15% reliability, the axial compression ratios $\nu_{15\%}$ for the exterior and interior beam were 0.058 and 0.084, corresponding to axial compression $N_{15\%}$ of 115.1 kN and 167.1 kN, respectively. For 85% reliability, the corresponding $\nu_{85\%}$ values were 0.110 and 0.155, with axial compression $N_{85\%}$ of 220.6 kN and 310.8 kN, respectively.

As noted before, in this study, $N_{15\%}$ was adopted for beam reinforcement optimization to avoid excessive reduction in

reinforcement that could prevent the beams from achieving the intended flexural strength under design-level seismic loading, thereby increasing fragility. In contrast, $N_{85\%}$ was adopted to estimate the restraint-induced force demands on columns and joints, providing a seismic safety margin to account for the beam axial compression effects.

5.2.3. Beam reinforcement optimization

Fig. 26 presents the axial-moment interaction curves for the first-story beams, and the corresponding reinforcement optimization results are summarized in Table 2. In this table, M_d denotes the code-based moment demand, M_0 is the flexural strength without axial compression, and M_N is the flexural strength accounting for restraint-induced axial compression. Prior to optimization, the axial compression $N_{15\%}$ resulted in beam flexural overstrength of 30.5% and 15.0% for the interior and exterior beams, respectively. Based on $N_{15\%}$ and M_d, the required longitudinal reinforcement ratios were recalculated using the axial–moment interaction relationship. Accordingly, the single-sided longitudinal reinforcement ratios ρ_l were reduced to 0.71% for the interior beams and 0.82% for the exterior beams. These values remain greater than the minimum reinforcement requirements specified by design codes, namely a reinforcement ratio exceeding 0.20% and a minimum reinforcement configuration of 2D14 bars. Overall, the optimized reinforcement layouts correspond to reductions of 25.3% and 13.7% in longitudinal reinforcement for the interior and exterior beams, respectively.

5.2.4. Column strengthening

Fig. 27 depicts the moment and shear demands for first-story columns obtained from code-based design and those adjusted following the procedures outlined in Section 4.3.2, based on the beam axial compression $N_{85\%}$. The shear amplification coefficient η_v were calculated as 2.22, 1.43, and 1.0 for the exterior, interior, and central columns, respectively, indicating an increasing beam axial compression effect from the frame center toward the edges. To accommodate the increased demands, the longitudinal reinforcement ratios ρ_{tot} for the exterior and interior columns were increased to 2.94% and 2.12%, representing relative increases of 79.7% and 29.4%, respectively.

In accordance with reinforcement detailing requirements [51], the transverse reinforcement was also enhanced to match the increased longitudinal bars, resulting in volume transverse reinforcement ratios ρ_v of 1.44% and 1.18% for the exterior and interior columns, respectively. Furthermore, the transverse reinforcement configuration in the joints must follow that of the adjacent column ends as specified by the standards [51]. Accordingly, the exterior and interior joints were concurrently strengthened in conjunction with the column reinforcement enhancements.

5.2.5. Joint strengthening

Fig. 28 compares the shear demands for the first-story joints obtained from code-based design and those adjusted following the procedures outlined in Section 4.3.3, based on the beam axial compression $N_{85\%}$. Owing to the beam reinforcement optimization, the increase in joint shear demand remained moderate, with the exterior, interior, and central joints experiencing increases of 56.6%, 28.0%, and 20.4%, respectively. The joint shear strengths calculated in accordance with design codes are also shown in Fig. 28. As the exterior and interior joints were already strengthened along with the columns, the resulting joint shear capacities were sufficient to resist the increased demands, and thus, no further joint strengthening was required.

Following application of the proposed design methodology, the first-story beam reinforcement was optimized to mitigate the overstrength issue caused by restraint-induced axial compression, while the first-story exterior and interior columns and joints were strengthened to resist the elevated seismic force demands.

5.3. Comparison with detailed analysis

5.3.1. Cyclic simulations

To assess the rationality and effectiveness of the proposed design methodology in addressing beam elongation restraint effects, cyclic analyses were performed in OpenSees [36] based on both the code design and the refined design using the proposed

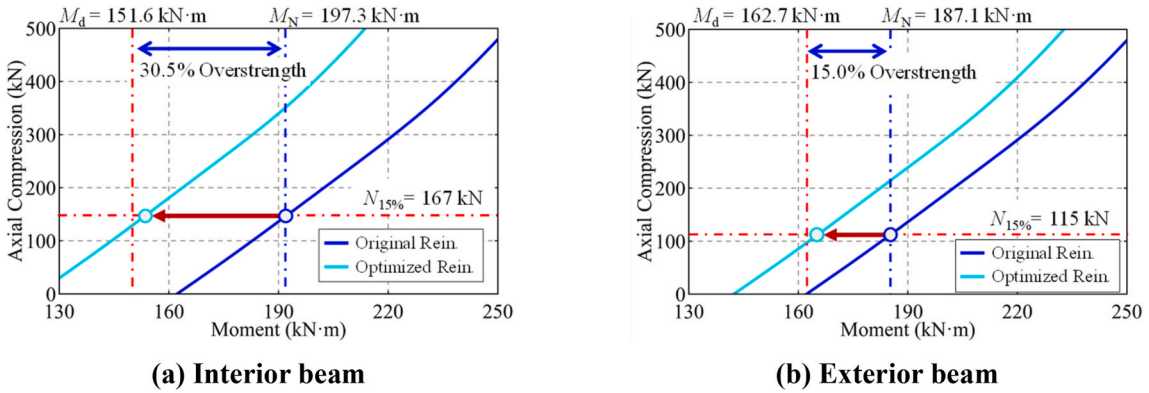


Fig. 26. Axial-moment interaction curves and reinforcement optimization for first-story beams.

Table 2
Beam reinforcement optimization under restraint-induced axial compression.

Position	M_d (kN)	$N_{15\%}$ (kN)	Before Optimization				After Optimization		
			Rein. Detail	ρ_l	M_0 (kN·m)	M_N (kN·m)	Rein. Detail	ρ_l	M_N (kN·m)
Interior	151.6	167	3D20	0.95%	163.6	197.3	2D18+1D16	0.71%	157.4
Exterior	162.7	115	3D20	0.95%	163.6	187.1	2D18+1D20	0.82%	165.5

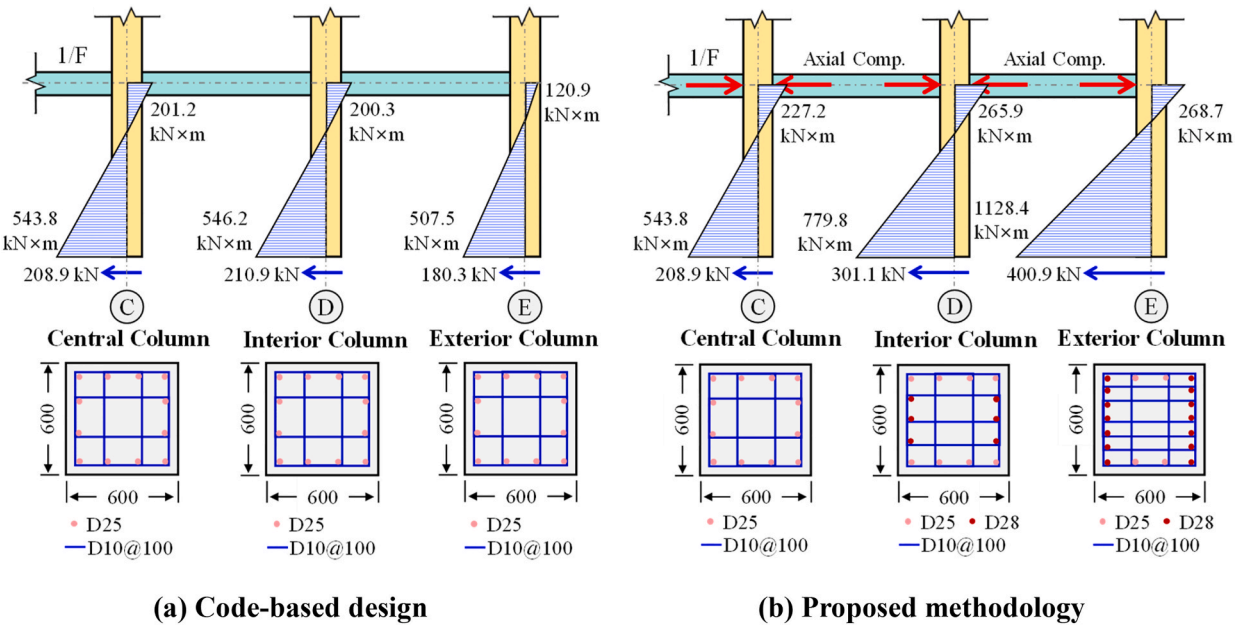


Fig. 27. Column force demands and reinforcement configuration in the first story.

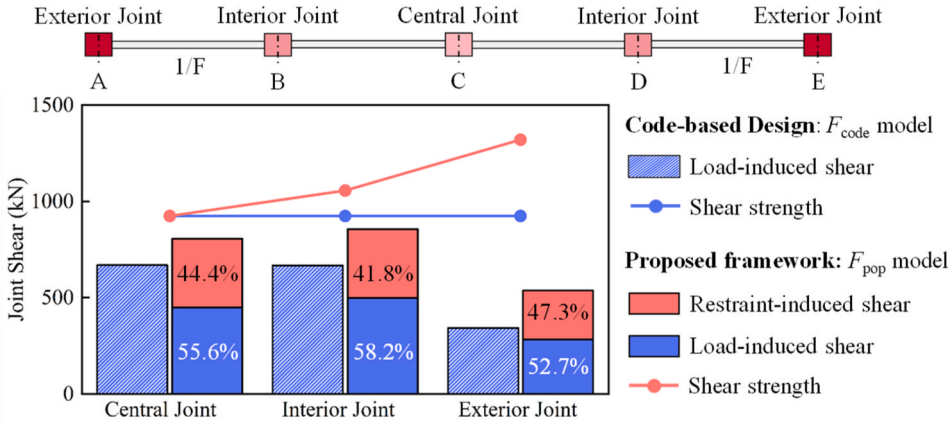


Fig. 28. Comparison of first-story joint shear demands and capacities.

methodology. Fig. 29 illustrates the finite element model employed, with the central beam-column assembly presented as a representative example. In this model, the beam and column elements were discretized using the same mesh scheme as that used for the test frame model shown in Fig. 4.

A triangular lateral load pattern was applied to the frame, and cyclic roof displacements were imposed on the top nodes of the central column. The displacement loading protocol consisted of increasing drift ratios of 0.1%, 0.2%, 0.5%, 1.0%, 1.5%, 2.0%, 3.0%, and 4.0%, with three cycles applied at each drift level. For clarity, the code-based frame is referred to as the F_{code} model, whereas the frame refined using the proposed methodology is denoted as the F_{prop} model.

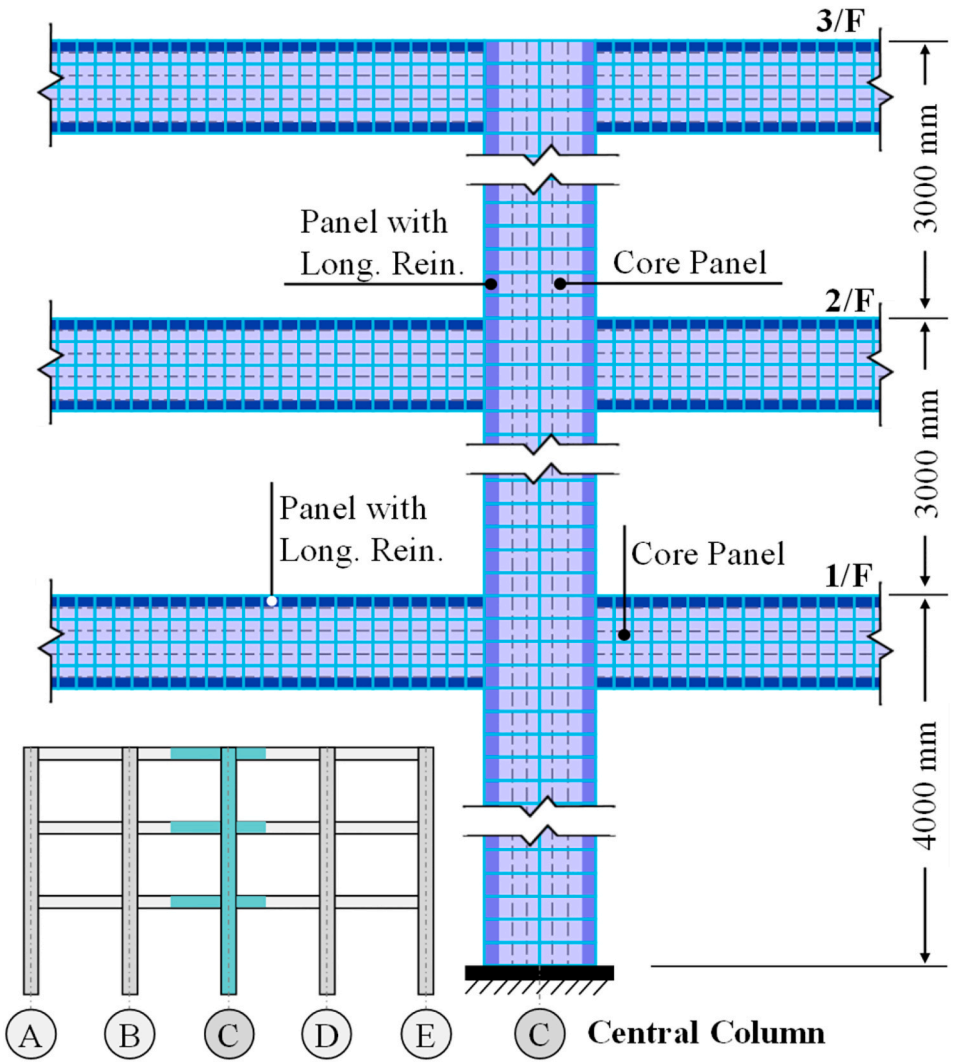


Fig. 29. Finite element model for the prototype frame.

5.3.2. Crack patterns and yield mechanisms

Fig. 30 compares the lateral hysteretic response for the F_{code} and F_{prop} models. Due to the enhanced reinforcement of the first-story exterior and interior columns, the F_{prop} model exhibited slightly improved lateral resistance and greater energy dissipation compared to the F_{code} model. On the other hand, Fig. 31 presents the crack patterns observed at the roof drift ratio of 4.0% and at the end of the loading protocol. In both models, pronounced flexural cracking developed at all beam ends, indicating full beam yielding and effective energy dissipation. Substantial flexural cracks were also observed at the base of the first-story columns, consistent with the expected failure mode that occurs after beam yielding. In contrast, only limited diagonal shear cracks appeared at the interior and central joints, suggesting that the strong-joint design objective was successfully achieved.

Additionally, the final crack patterns reflected the deformation modes induced by beam elongation. Due to the restraint imposed by adjacent columns, axial compression developed in the beams, which in turn elevated the force demands on columns and joints. This mechanism resulted in one-directional flexural cracks at the ends of exterior columns connected to the first-story beams under cyclic loading, consistent with experimental observations. Furthermore, these deformation patterns were in agreement with those predicted using the thermal analogy method shown in Fig. 25, confirming the ability of the proposed method to capture elongation-induced deformation modes without requiring nonlinear analysis.

Fig. 32 presents the yield mechanisms of the two models focusing on the first story. In both cases, beam yielding occurred prior to column yielding, aligning with the strong-column/weak-beam design philosophy. The story drift ratios corresponding to beam yielding were 0.0024 and 0.0021 for the F_{code} and F_{prop} models, respectively, with the lower value in the F_{prop} model attributed to its optimized beam reinforcement. Due to the more pronounced influence of restraint-induced axial compression on the exterior columns, yielding initiated in the exterior columns in both models, followed by the interior and central columns. The drift ratios corresponding to yielding at the base of all first-story columns were 0.0047 and 0.0051 for the F_{code} and F_{prop} models, corresponding to ERD values of

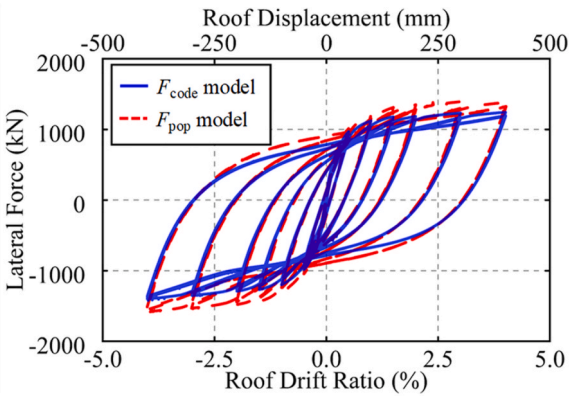


Fig. 30. Comparison of lateral hysteretic response for F_{code} and F_{prop} models.

1.96 and 2.43, respectively. Notably, both ERD values were within the 15%–85% reliability range, supporting the rationality of selecting ERD values corresponding to 18% and 85% reliability levels for seismic design.

5.3.3. Beam hysteretic response

Given the structural symmetry, the interior and exterior beams between Grid Lines C and E were selected to illustrate the hysteretic response. Fig. 33 shows the relationships between the restraint-induced axial force and the beam elongation. The results indicate that the first-story beams were subjected to axial compression, while the second- and third-story beams experienced comparable levels of axial tension. These observations are consistent with the axial force distributions predicted by the thermal analogy method.

To quantify the axial restraint stiffness K_r, an elasto-plastic bilinear backbone curve was fitted to the hysteretic responses based on energy equivalence. The relative errors between the K_r values estimated by the thermal analogy method and those derived from numerical simulations are indicated in parentheses. All errors remained within 20%, demonstrating the adequacy and robustness of the proposed estimation method.

Compared with the F_{code} model, the F_{prop} model exhibited higher axial compression and greater K_r in the first-story beams. This improvement is attributed to delayed column yielding resulting from reinforcement enhancements, which provided more effective restraint against beam elongation. Furthermore, the maximum axial compression in the first-story beams of both models fell within the range bounded by $N_{15\%}$ and $N_{85\%}$, which were employed for beam reinforcement optimization and column/joint strengthening, respectively.

Fig. 34 depicts the lateral load-drift hysteretic responses of the first-story beams subjected to restraint-induced axial compression. In the F_{code} model, the axial compression led to notable beam overstrength, ranging from 18.7% to 20.9% for exterior beams and from 37.5% to 37.9% for interior beams. In contrast, the F_{prop} model, incorporating beam reinforcement optimization, achieved notable reductions in overstrength, with values ranging from 11.1% to 10.6% for exterior beams and 16.3%–17.4% for interior beams. This residual overstrength primarily results from the actual axial compression exceeding the $N_{15\%}$ adopted in the optimization process. Nevertheless, maintaining a moderate level of overstrength is essential to ensure that the beams possess adequate flexural strength under design-level seismic loading, thereby preventing excessive vulnerability due to over-optimization. Notably, the reduced overstrength levels in the F_{prop} model remained within the safety margin provided by the design code, which specifies a moment amplification factor $\eta_c = 1.2$ in Eq. (18) [51]. These results confirm the effectiveness of the proposed reinforcement optimization strategy in mitigating overstrength within a rational range.

5.3.4. Column shear demands

To evaluate the column force demands, the first-story central, interior, and exterior columns between Grid Lines C and E were examined. Fig. 35 shows the shear force composition at critical loading stages, including beam yielding, first-story column base yielding, and the peak shear force observed during analysis. The results indicate an increase in column shear force from the frame center toward the edges, primarily due to the additional shear generated by restraint-induced beam axial compression. For the exterior columns, this restraint effects accounted for 44.4%–56.4% of the total shear force.

Current seismic design codes do not however account for the beam axial compression effects in evaluating the column force demands. Consequently, the shear forces for the interior and exterior columns were underestimated, failing to reflect the actual distribution pattern. Specifically, the code assigned the lowest shear demand to exterior columns, despite these columns experiencing the highest shear forces in the analysis. This mismatch led to an underestimation of 15.0% and 49.7% at the beam and column yielding stages, respectively.

Although the prototype frame was designed for a seismic Intensity 9, wherein the force demands at the base of first-story columns were amplified by a factor of 1.7 as per code provisions [51], this amplification only partially mitigated this underestimation. For structures designed under lower seismic intensity levels, where smaller amplification factors are applied, the severity of underestimation would be more pronounced. This deficiency increases the risk of premature column failure, especially in exterior columns,

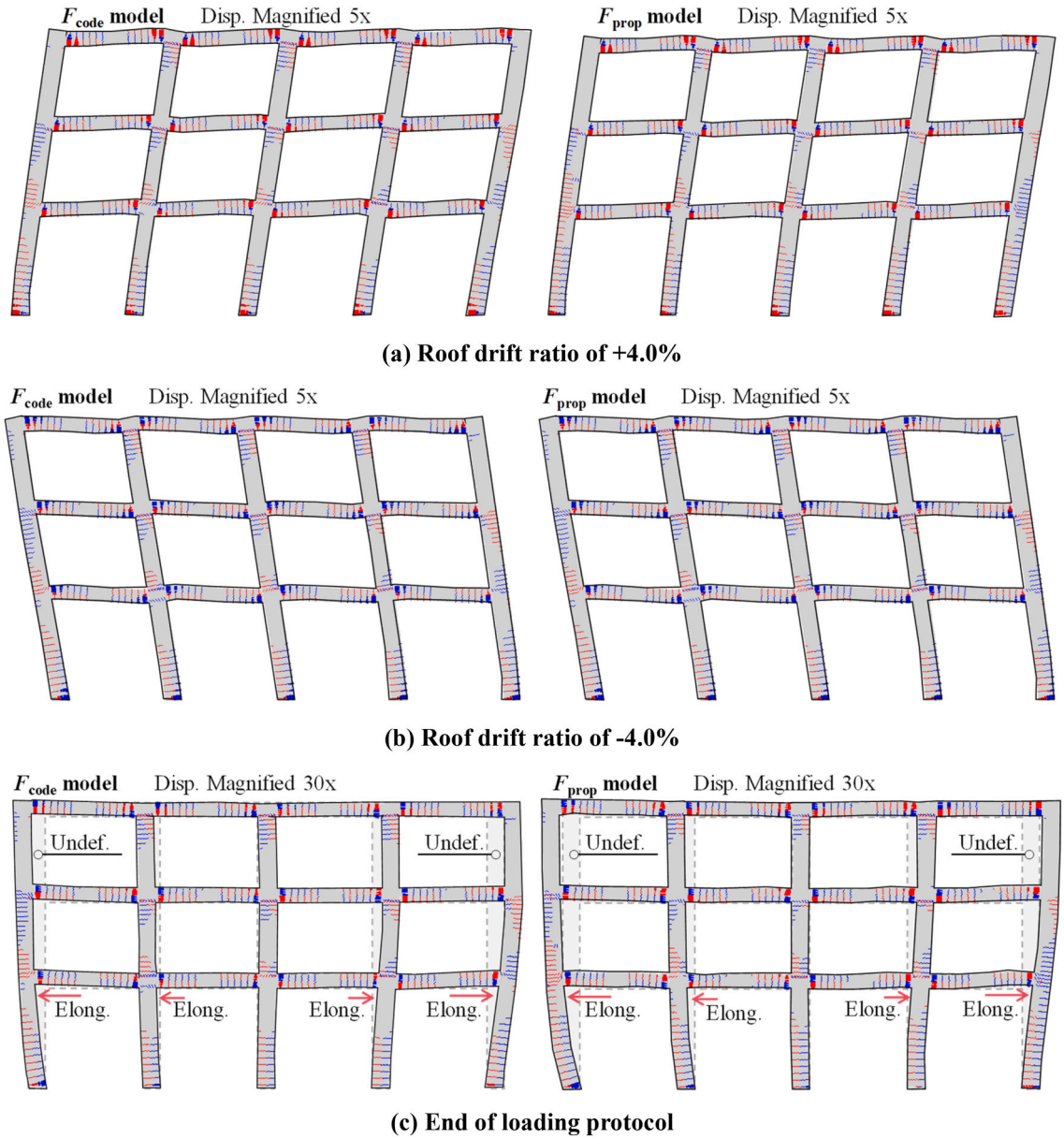


Fig. 31. Comparison of crack patterns between F_{code} and F_{prop} models.

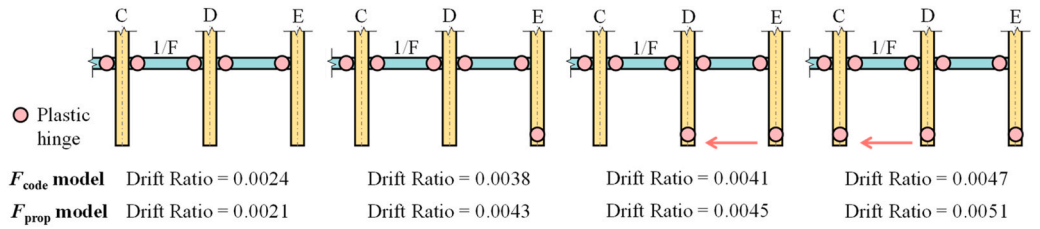


Fig. 32. Yield sequence of first-story components and associated drift ratios.

thereby compromising the intended strong-column/weak-beam design philosophy.

In contrast to code design, the proposed design methodology explicitly accounts for the beam axial compression effects on evaluating column force demands. The adjusted design values not only successfully captured the distribution pattern of column shear

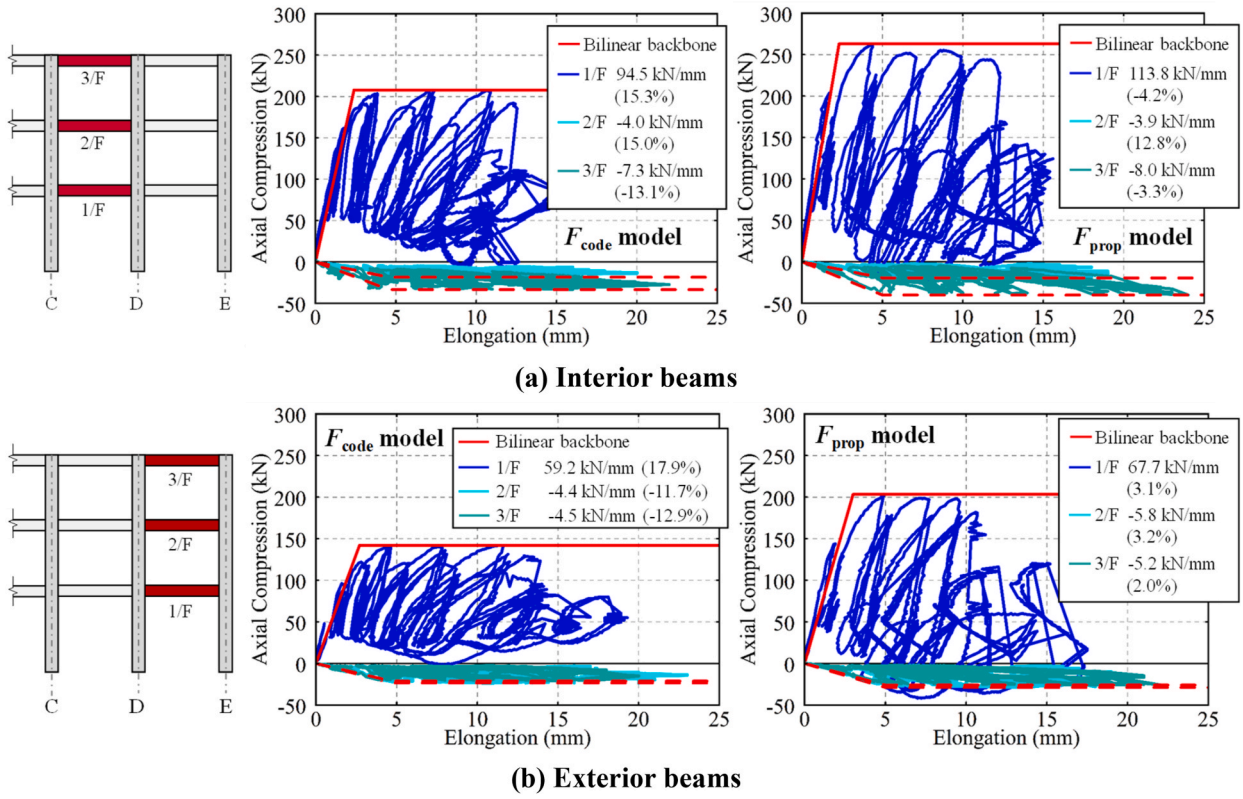


Fig. 33. Hysteretic axial force–elongation response of beams.

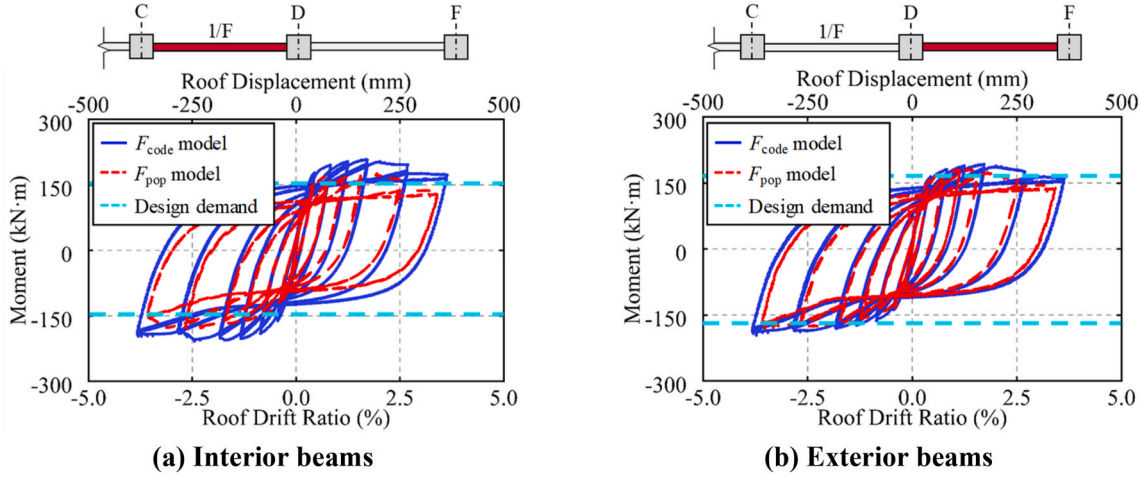


Fig. 34. Lateral load-drift hysteretic response of the first-story beams subjected to axial compression.

forces observed in simulations but also provided a safety margin This margin arose from adopting $N_{85\%}$ axial compression with a 15% exceedance probability for force demand estimation, which was higher than the actual compression levels encountered in the analysis. These results confirm the effectiveness of the proposed methodology in capturing the beam restraint effects on column shear demands in seismic design.

5.3.5. Joint shear demands

Similarly, the central, interior, and exterior joints in the first story between Grid Lines C and E were selected to evaluate the joint shear demands. Fig. 36 presents the joint shear force composition at critical loading stages, including beam yielding, first-story column

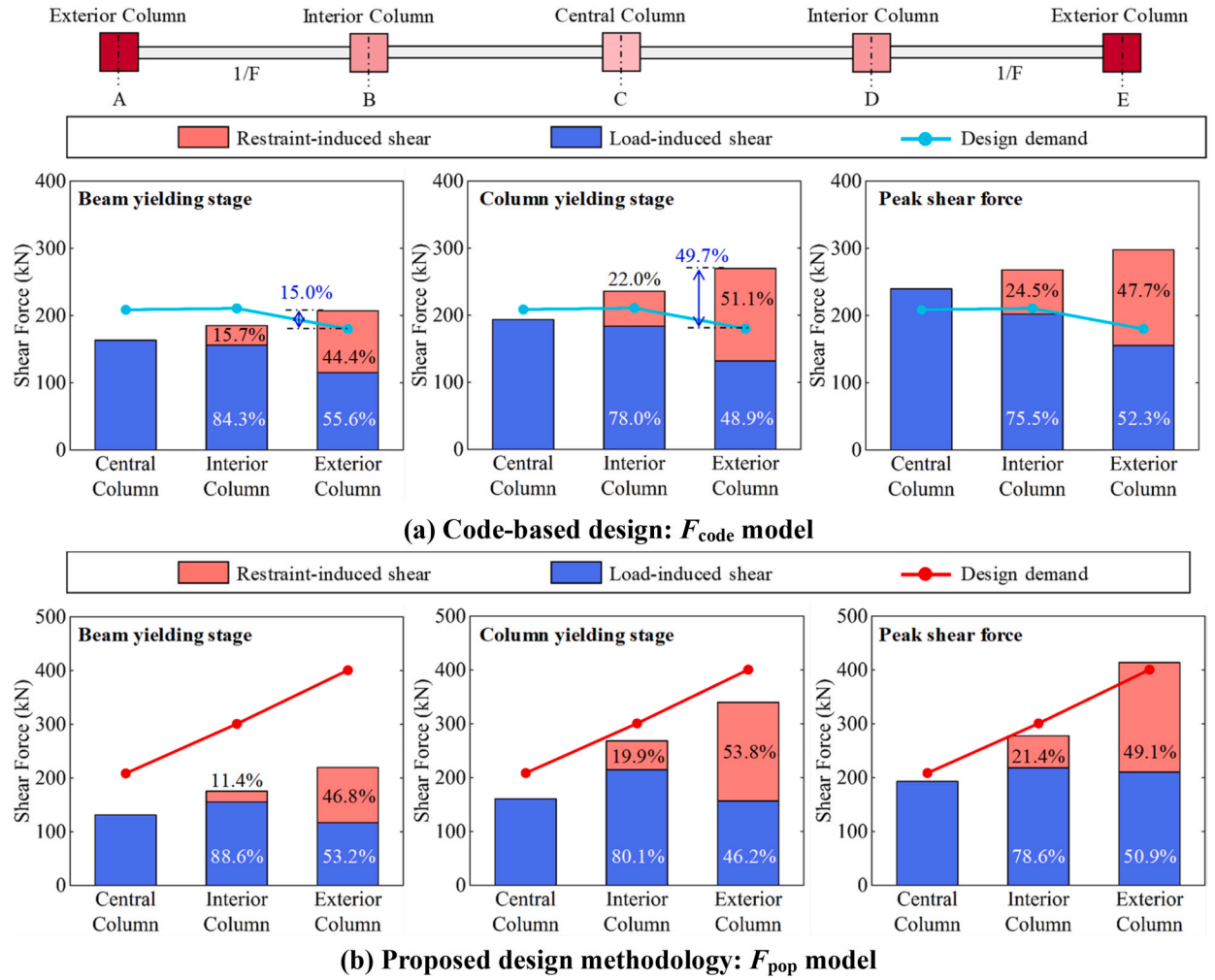


Fig. 35. Shear force composition for the first-story columns at critical loading stages.

base yielding, and the peak shear force observed during the analysis. The results reveal that restraint-induced beam axial compression significantly increased the shear demands on exterior joints, contributing 30.3%–45.4% of their total shear force. However, the overall distribution pattern remained unchanged, with exterior joints still experiencing the lowest shear forces compared to the interior and central joints.

Due to the optimized beam reinforcement in the F_{prop} model, joint shear forces were generally lower than those in the F_{code} model, particularly in the central and interior joints, where reductions of 18.4%–27.7% were observed. Moreover, the column reinforcement enhancements in the F_{prop} model facilitated the development of higher beam axial compression, thereby increasing the proportion of restraint-induced shear contribution.

Although the design code applies a shear amplification factor as specified in Eq. (20), the joint shear forces observed in the simulations exceeded the corresponding code-based design values. In contrast, the adjusted design demands provided by the proposed methodology successfully enveloped the actual joint shear forces, corroborating its ability to incorporate the beam restraint effects in the estimation of joint shear demands.

6. Conclusions

This study proposed a seismic design methodology for RC frame structures that explicitly accounts for the restraint effects to beam hysteresis elongation. The methodology comprises four sequential steps: (i) evaluation of beam axial restraint stiffness, (ii) determination of restraint-induced axial compression, (iii) beam reinforcement optimization through axial-moment interaction, and (iv) column and joint strengthening to resist the resulting force demands. The main contributions and findings are summarized as follows.

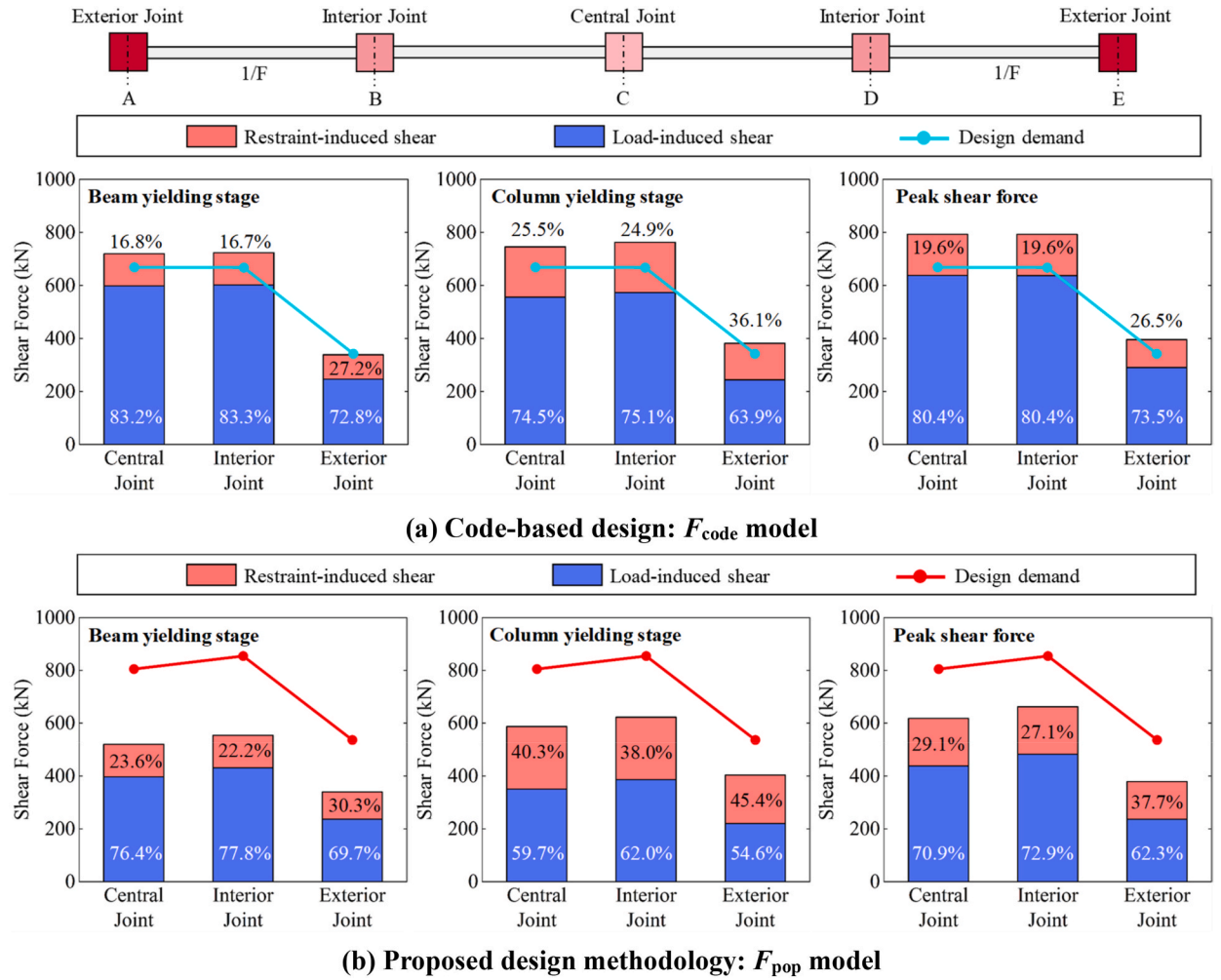


Fig. 36. Shear force composition for the first-story joints at critical loading stages.

1. A thermal analogy approach was proposed to efficiently estimate the beam axial restraint stiffness. Validation against the results from detailed cyclic analysis for multi-story RC frames confirmed its capability to capture elongation-induced deformation patterns and beam axial force distributions, resulting in reliable estimation of the restraint stiffness.
2. A prediction model for restraint-induced beam axial compression was developed by introducing a normalized parameter, denoted the effective restraint ductility (ERD), which accounts for the restraint degradation effect caused by column yielding. The model was calibrated against detailed simulations, and was shown to provide reliable estimation of the axial compression across a wide range of beam parameters and restraint conditions.
3. It was shown through detailed cyclic simulations on multi-story RC frames that the restraint-induced axial compression leads to beam flexural overstrength and imposes substantial additional force demands on adjacent components. The proportion of restraint-induced shear increased from the frame center toward the edges, accounting for 44.4%-73.5% of the total shear in exterior columns and 30.3%-47.7% in exterior joints. Code-based designs fail to capture these effects, resulting in 37.5%–37.9% flexural overstrength in interior beams and underestimating exterior column shear demands by up to 49.7% at the column yielding stage, despite incorporating various capacity design amplification factors.
4. The proposed design methodology was applied to a prototype multi-story RC frame, with comparisons against detailed cyclic analysis confirming its effectiveness in mitigating excessive beam overstrength and capturing restraint-induced force demands on columns and joints. By dealing with the restraint effects through beam reinforcement optimization and column-joint strengthening, the proposed methodology enables the mobilization of the intended strong-column/weak-beam and strong-joint mechanisms, thereby enhancing the ductility, energy dissipation, and overall seismic performance of RC frames.

As ERD varies with frame configuration, the proposed design methodology was applied to a prototype multi-story RC frame using ERD values corresponding to 15% reliability for beam optimization and 85% reliability for column–joint strengthening. While this reliability combination proved effective for the prototype frame, future studies should extend the evaluation to a wider range of frame

configurations through seismic resilience analysis in order to identify optimal ERD reliability levels. In addition, the proposed axial compression prediction model is directly applicable to RC frames employing seated precast floor systems for which slab–beam interaction is limited, yet it also provides a fundamental basis towards future explicit extension of the methodology to integral slab-frame systems.

CRediT authorship contribution statement

Zi-Nan Wu: Writing – original draft, Visualization, Validation, Software, Methodology, Investigation, Funding acquisition, Formal analysis, Data curation, Conceptualization. **Xiao-Lei Han:** Supervision, Resources, Methodology, Investigation, Conceptualization. **Ahmed Y. Elghazouli:** Writing – review & editing, Supervision, Resources, Project administration, Methodology, Funding acquisition, Conceptualization. **Cunbiao Huang:** Visualization, Investigation, Formal analysis, Data curation.

Declaration of competing interest

The authors declare that they have no known competing financial interests or personal relationships that could have appeared to influence the work reported in this paper.

Acknowledgments

Funding from the China Postdoctoral Science Foundation (2024M760958) is gratefully acknowledged.

Data availability

Data will be made available on request.

References

[1] G. Dong, R. Garcia, K. Pilakoutas, et al., A review of optimum seismic design of RC frames: state-of-the-art, challenges and future directions, Eng. Struct. 315 (2024) 118455.
[2] T.K. Das, S. Choudhury, P. Das, Correlation between seismic performance levels and damage index for regular RC frame buildings designed using the unified performance-based design method, J. Build. Eng. 96 (2024) 110565.
[3] H. Zhang, X. Cheng, Y. Li, et al., Rapid seismic damage state assessment of RC frames using machine learning methods, J. Build. Eng. 65 (2023) 105797.
[4] T.S. Eom, H.G. Park, Elongation of reinforced concrete members subjected to cyclic loading, J. Struct. Eng. 136 (9) (2010) 1044–1054.
[5] R.V. Mehrabani, V. Sigrist, Elongation of reinforced concrete plastic hinges subjected to reversed cyclic loading, J. Struct. Eng. 141 (8) (2015) 04014188.
[6] Z.N. Wu, Y. Dong, X.L. Han, et al., Hysteresis elongation behavior of RC beams failing in different modes: experimental investigation and numerical modelling using smeared crack approach, Eng. Struct. 329 (2025) 119807.
[7] R.C. Fenwick, L.M. Megget, Elongation and load deflection characteristics of reinforced concrete members containing plastic hinges, Bull NZNSEE 26 (1) (1993) 28–41.
[8] J.Y. Lee, F. Watanabe, Predicting the longitudinal axial strain in the plastic Hinge regions of reinforced concrete beams subjected to reversed cyclic loading, Eng. Struct. 25 (7) (2003) 927–939.
[9] S. Kokusho, S. Hayashi, A. Wada, et al., Behaviors of reinforced concrete beam subjected to the axial restriction of deformation, Proc., 9th World Conf. on Earthq Eng. Tokyo, Japan (1988).
[10] E.I. Yang, S.T. Yi, S. Morita, Effect of axial restraint on flexural and shear behaviour of high-strength concrete members, Mag. Concr. Res. 56 (2) (2004) 63–72.
[11] L. Wang, Y. Tian, W. Luo, et al., Seismic performance of axially restrained reinforced concrete frame beams, J. Struct. Eng. 145 (5) (2019) 04019019.
[12] B. Mihaylov, A. Trandafir, X. Palios, et al., Effect of axial restraint and loading history on the behavior of short reinforced concrete coupling beams, ACI Struct. J. 118 (78) (2021) 71–82.
[13] J. Park, E. Strepelias, N. Stathas, et al., Application of hybrid simulation method for seismic performance evaluation of RC coupling beams subjected to realistic boundary condition, Earthq. Eng. Struct. Dynam. 50 (2) (2021) 375–393.
[14] K.K. Anaraki, J.W. Wallace, Analytical model for RC coupling beam considering axial restraint, Eng. Struct. 322 (2025) 119086.
[15] C.J. Motter, Reinforced concrete coupling beams with axial restraint, ACI Struct. J. 122 (1) (2025) 35–49.
[16] W. Luo, L. Jiang, C. Lei, et al., Effects of axial restraints on beam flexural and joint shear behaviors in reinforced concrete frames under seismic loading, J. Earthq. Eng. 27 (1) (2023) 121–141.
[17] H.E. Zerbe, A.J. Durrani, Seismic response of connections in two-bay R/C frame subassemblies, J. Struct. Eng. 115 (11) (1989) 2829–2844.
[18] R.C. Fenwick, B.J. Davidson, Elongation in ductile seismic-resistant reinforced concrete frames, ACI Spec. Publ. 157 (1995) 143–170.
[19] J. Kim, J. Stanton, G. MacRae, Effect of beam growth on reinforced concrete frames, J. Struct. Eng. 130 (9) (2004) 1333–1342.
[20] J.H. Kim, S.H. Choi, S.J. Han, et al., Effect of beam elongation phenomenon on lateral load resistance of RC frame, J. Build. Eng. 65 (2023) 105764.
[21] C.B. Haselton, A.B. Liel, S.C. Taylor-Lange, et al., Calibration of model to simulate response of reinforced concrete beam-columns to collapse, ACI Struct. J. 113 (6) (2016) 1141–1152.
[22] C.S. Lee, J.S. Jeon, Adaptive hysteretic model for reinforced concrete columns including variations in axial force and shear span length, Earthq. Eng. Struct. Dynam. 50 (15) (2021) 4001–4031.
[23] B. Todorov, A.H.M.M. Billah, Machine learning driven seismic performance limit state identification for performance-based seismic design of bridge piers, Eng. Struct. 255 (2022) 113919.
[24] GB 50010-2010, Code for Design of Concrete Structures, China Architecture & Building Press, 2015.
[25] J.Y. Lee, F. Watanabe, Predicting the longitudinal axial strain in the plastic Hinge regions of reinforced concrete beams subjected to reversed cyclic loading, Eng. Struct. 25 (7) (2003) 927–939.
[26] NZS 3101.2:2006 (incorporating Amendments 1–3), Concrete Structures Standard. Standards New Zealand, 2017.
[27] M.H. Scott, G.L. Fenves, Plastic Hinge integration methods for force-based beam–column elements, J. Struct. Eng. 132 (2) (2006) 244–252.
[28] Z.N. Wu, X.L. Han, A. He, et al., Machine learning-based adaptive degradation model for RC beams, Eng. Struct. 253 (2022) 113817.
[29] J.C. Lin, X.L. Han, Z.N. Wu, et al., Development and application of out-of-plane deformable X-shaped brace for energy dissipation and thermal stress mitigation: an experimental and numerical study, Thin-Walled Struct. 203 (2024) 112186.
[30] B.H.H. Peng, R.P. Dhakal, R.C. Fenwick, et al., Multispring Hinge element for reinforced concrete frame analysis, J. Struct. Eng. 139 (4) (2013) 595–606.

[31] A.N. Hanoon, M.S. Jaafar, S.R. Al Zaidee, et al., Effectiveness factor of the strut-and-tie model for reinforced concrete deep beams strengthened with CFRP sheet, J. Build. Eng. 12 (2017) 8–16.
[32] L. Xiong, Q. Luo, J. He, et al., Shear strength prediction of interior RC column and steel beam composite joints using the modified softened strut-and-tie model, J. Build. Eng. 88 (2024) 109250.
[33] F.J. Vecchio, M.P. Collins, The modified compression-field theory for reinforced concrete elements subjected to shear, ACI J 83 (2) (1986) 219–231.
[34] X.B.D. Pang, T.T.C. Hsu, Fixed angle softened truss model for reinforced concrete, ACI Struct. J. 93 (2) (1996) 196–208.
[35] Q. Qi, L. Jiang, C. Shao, et al., Hysteretic behavior modeling of RC walls considering axial-flexure-shear interaction, J. Build. Eng. 111 (2025) 113628.
[36] F. McKenna, M.H. Scott, G.L. Fenves, Nonlinear finite-element analysis software architecture using object composition, J. Comput. Civ. Eng. 24 (1) (2010) 95–107.
[37] K. Kolozvari, K. Orakcal, J.W. Wallace, New opensees models for simulating nonlinear flexural and coupled shear-flexural behavior of RC walls and columns, Comput. Struct. 196 (2018) 246–262.
[38] N. Ning, W. Qu, P. Zhu, Role of cast-in situ slabs in RC frames under low frequency cyclic load, Eng. Struct. 59 (2014) 28–38.
[39] C.N. López, F. Rojas, L.M. Massone, Membrane fiber element for reinforced concrete walls–the benefits of macro and micro modeling approaches, Eng. Struct. 254 (2022) 113819.
[40] K. Orakcal, L.M. Massone, D. Ulugtekin, A hysteretic constitutive model for reinforced concrete panel elements, Int. J. Concr. Struct. Mater. 13 (2019) 51.
[41] G.A. Chang, J.B. Mander, Seismic Energy Based Fatigue Damage Analysis of Bridge Columns: Part I-Evaluation of Seismic Capacity, National Center for Earthquake Engineering Research, Buffalo, NY, 1994.
[42] K. Orakcal, J.W. Wallace, Flexural modeling of reinforced concrete walls-experimental verification, ACI Mater. J. 103 (2) (2006) 196–206.
[43] M. Menegotto, P.E. Pinto, Method of analysis for cyclically loaded reinforced concrete plane frames including changes in geometry and non-elastic of elements under combined normal force and bending, IABSE Symposium (1973).
[44] N. Ning, W. Qu, P. Zhu, Effect of cast in-situ slabs on seismic performance of spatial RC frames, J. Build. Struct. 46 (2) (2014) 72–77 (in Chinese).
[45] Z.N. Wu, A.Y. Elghazouli, X.L. Han, et al., Assessment and design of restrained reinforced concrete beams subjected to hysteresis elongation effects, Eng. Struct. 346 (2026) 121408.
[46] Hazus-MH 6.1 Earthquake Model Technical Manual, Federal Emergency Management Agency, 2024.
[47] C. Xiong, X. Lu, H. Guan, et al., A nonlinear computational model for regional seismic simulation of tall buildings, Bull. Earthq. Eng. 14 (4) (2016) 1047–1069.
[48] X. Lu, Y. Tian, G. Wang, et al., A numerical coupling scheme for nonlinear time history analysis of buildings on a regional scale considering site-city interaction effects, Earthq. Eng. Struct. Dynam. 47 (13) (2018) 2708–2725.
[49] H. Bu, H. Jiang, Y. Sanada, A unified simplified numerical model for large-scale regional seismic simulation of building structures, J. Build. Eng. 102 (2025) 112004.
[50] C. Xiong, X. Lu, X. Lin, et al., Parameter determination and damage assessment for THA-based regional seismic damage prediction of multi-story buildings, J. Earthq. Eng. 21 (3) (2017) 461–485.
[51] GB 50011-2010, Code for Seismic Design of Buildings, China Architecture & Building Press, 2016.